

# Theoretical analysis of zirconium oxynitride/water interface using neural network potential

Akitaka Nakanishi,<sup>\*,†</sup> Shusuke Kasamatsu,<sup>‡</sup> Jun Haruyama,<sup>†</sup> and Osamu Sugino<sup>†</sup>

<sup>†</sup>*The Institute for Solid State Physics, The University of Tokyo, 5-1-5 Kashiwanoha,  
Kashiwa-shi, Chiba 277-8581, Japan*

<sup>‡</sup>*Faculty of Science, Yamagata University, 1-4-12 Kojirakawa, Yamagata-shi, Yamagata  
990-8560, Japan*

E-mail: nakanishi@issp.u-tokyo.ac.jp

## Abstract

Zr oxides and oxynitrides are promising candidates to replace precious metal cathodes in polymer electrolyte fuel cells. Oxygen reduction reaction activity in this class of materials has been correlated with the amount of oxygen vacancies, but a microscopic understanding of this correlation is still lacking. To address this, we simulate a defective  $\text{Zr}_7\text{O}_8\text{N}_4/\text{H}_2\text{O}$  interface model and compare it with a pristine  $\text{ZrO}_2/\text{H}_2\text{O}$  interface model. First, ab initio replica exchange Monte Carlo sampling was performed to determine defect segregation at the surface in the oxynitride slab model, then molecular dynamics accelerated by neural network potentials was used to perform 1000 of 500 ps-long simulations to attain sufficient statistical accuracy of the solid/liquid interface structure. The presence of oxygen vacancies on the surface was found to clearly modify the local adsorption structure: water molecules were found to adsorb preferentially on Zr atoms surrounding oxygen vacancies, but not on the oxygen vacancies themselves.

The fact that oxygen vacancy sites are free from poisoning by water molecules may explain the activity enhancement in defective systems. The layering of water molecules was also modified considerably, which should influence the proton and O<sub>2</sub> transport near the interfaces which is another parameter that determines the overall activity.

## Introduction

Polymer electrolyte fuel cells (PEFCs) are attracting attention as energy conversion devices, and their performance depends on the catalytic activity of the oxygen reduction reaction (ORR) taking place on the cathode side. Currently, Pt or its alloys are used as the ORR catalyst owing to their high catalytic activity, although durability and cost issues are hindering the wide-spread production and use of PEFCs.<sup>1</sup>

Zr oxides<sup>2-4</sup> and Ti oxides<sup>5-8</sup> are promising candidates to replace Pt as electrocatalysts due to their high durability, low cost, and high catalytic activity obtained by introducing defects such as oxygen vacancies (V<sub>O</sub>s) and oxygen-nitrogen substitutions (N<sub>O</sub>s).<sup>9,10</sup> Previous experimental studies have shown that the catalytic activity correlates with the amount of V<sub>O</sub>s in ZrO<sub>2</sub>,<sup>2,11,12</sup> suggesting that V<sub>O</sub>s are the active centers for the ORR. The presence of oxynitride phases such as Zr<sub>2</sub>ON<sub>2</sub> ( $\gamma$  phase) and Zr<sub>7</sub>O<sub>8</sub>N<sub>4</sub> ( $\beta$  phase), which can be regarded as fluorite-structured ZrO<sub>2</sub> with vacancy ordering,<sup>13,14</sup> have also been reported in catalytically active samples.<sup>15</sup> However, the reaction pathways, rate-determining steps, and various other aspects of the ORR remain unknown.

To the best of our knowledge, there have not been many theoretical studies on the ORR activity of defective oxide surfaces compared to pristine ones.<sup>16-18</sup> One such work is by Muhammady et al., who performed an exhaustive search for ORR intermediate structures and calculated the corresponding ab initio free energy diagrams on tetragonal ZrO<sub>2</sub>(101) surfaces with V<sub>O</sub> and N<sub>O</sub> based on the computational hydrogen electrode (CHE) model.<sup>18,19</sup> The results suggest that Zr atoms and V<sub>O</sub> on the surface do not differ significantly in terms of local site activity, in apparent contrast to the experimental literature. However, the influence

of the solvent was only considered through solvation correction energies, and neither solvent nor adsorbed water molecules were considered explicitly. This means that possibility of poisoning of active sites by the solvent is ignored. In addition, the CHE model does not contain contributions from finite-temperature dynamics of the intermediates.

Thus, the natural way to resolve the abovementioned discrepancies between theory and experiment would be to accurately consider explicit solvent effects and dynamics using ab initio molecular dynamics (AIMD). However, the high computational cost is a major problem, especially for models with a large number of atoms in the unit cell such as catalysts with defects, or when dynamic properties such as proton diffusion are studied which requires simulations of 1 ns or longer. In recent years, this issue has been solved to some extent through the advent of machine learning potentials (MLPs), which enable more efficient molecular dynamics calculations while maintaining the same level of accuracy as ab initio calculations.<sup>20</sup> Numerous works have been reported that employ MLPs to study adsorption structures and proton transfer at the interfaces of pristine solids and water.<sup>21–36</sup> However, application to complex and defective oxides are still lacking, partially due to difficulties in obtaining a stable MLP that can treat complex solid/liquid interfaces with a large number of distinct chemical environments. It is often the case that simulations ‘blow up’ when the system wanders into regions of space that the MLP has not been trained on.

Another issue in modeling of complex oxides is in determining the ion ordering. In the case of zirconium oxynitrides, two stoichiometric phases are known with vacancy ordering in the bulk as mentioned above, but the anion ordering is still under debate because x-ray diffraction cannot be used to separate oxygen and nitrogen sites. The situation is even more complicated when considering surfaces, as there is no experimental information on segregation of  $N_O$  or  $V_O$  and whether vacancy ordering persists at the surface. Such segregation would be decisive in determining the surface activity and stability, but theoretical prediction is challenging due to the combinatorial explosion in the number of possible configurations. Molecular dynamics cannot solve this issue because ion and defect arrangements in complex oxides are very slow

to relax and are determined by firing or sintering processes whose time scales are beyond the reach of atomistic simulations.

In this work, we apply recently developed methodologies to solve the above issues and investigate the structure of water molecules at the interface between water and defective oxide catalysts, as a first step towards understanding the effects of defects and solvents on ORR activity. Examples of such effects include the influence of water layering on proton transfer and the poisoning of  $O_2$  adsorption sites by water. We compare zirconium oxynitride with  $Zr_7O_8N_4$  composition to  $ZrO_2$ , where the former can be considered as  $ZrO_2$  with a large number of  $N_O$  and  $V_O$  defects, with one  $V_O$  for every two  $N_O$  to satisfy formal ion charge neutrality. First, ab initio replica exchange Monte Carlo simulation accelerated by active learning of a neural network configuration energy model<sup>37-39</sup> was carried out to obtain a  $Zr_7O_8N_4$  slab model with thermodynamically stable  $N_O$  and  $V_O$  segregation profiles. Then, neural network potentials (NNPs)<sup>40,41</sup> that reproduce ab initio calculations for interfaces of water and  $ZrO_2/Zr_7O_8N_4$  were constructed using this surface slab model through an iterative active learning approach detailed in the next section. Once a stable NNP was obtained, hundreds of nanosecond-long trajectories were generated using NNP molecular dynamics (NNPMD) to study water molecule adsorption on the surfaces of  $Zr_7O_8N_4$  and  $ZrO_2$ . The possibility of the  $V_O$  as catalytically active sites is discussed by comparing the two systems.

## Model and Methods

### Surface slab models

In this work, we model the tetragonal zirconia and zirconium oxynitride surfaces which correspond to the (111) surface in the cubic fluorite setting. This corresponds to the (101) orientation in tetragonal zirconia (whose structure is slightly distorted from the fluorite) and the (???) orientation of the orthorhombic  $\beta$  phase. This surface was chosen because the (111) facet has been predicted to be most stable in pure zirconia and is often observed

in experiments. The (111) orientation in the fluorite setting consists of neutral units of  $-(\text{O}-\text{Zr}-\text{O})-(\text{O}-\text{Zr}-\text{O})-\dots$ ; here, we consider  $n$  repetitions of the (O-Zr-O) unit. We employ the in-plane unit cell with  $a = b = 9.542394 \text{ \AA}$  shown in Fig. 1 (a), which results in  $2n$  Zr sites and  $2n$  O sites, where the latter can be occupied by O,  $\text{N}_\text{O}$  or  $\text{V}_\text{O}$  in the oxynitride. For the oxynitride slab, replica exchange Monte Carlo (RXMC) sampling using a neural network configuration energy model is first performed without water to simulate nitrogen and oxygen vacancy segregation near the surface as detailed in Sec. 2.2. One of the lowest energy configurations found is used in subsequent NNPM simulation. Figure 1 (b) shows the interface models simulated by NNPM where water molecules were placed on top of the surface of the pristine tetragonal  $\text{ZrO}_2$  surface and the oxynitride surface from RXMC sampling. The interface model contains a random arrangement of water molecules in a unit cell with an additional vacuum layer of  $15 \text{ \AA}$ . The number of water molecules was set to 21 per calculation cell, which corresponds to about three layers of water.

To improve the thermodynamic sampling of water structures, we performed numerous NNPM runs with different initial water configurations. The following procedure was employed to prepare initial configurations that are not correlated with each other. First, the xy-coordinates of the water molecules were set so that the oxygen of the water molecules was above one of the atoms of the slab and the dipole moment of the water molecules was parallel to the x-axis. Then, the 21 water molecules were randomly assigned to three different groups of seven water molecules each, and depending on the group, the z-component of the atomic coordinates was set to a value of 3, 6, and  $9 \text{ \AA}$  higher than the z-coordinate of outermost surface layer of the oxide and oxynitride. We also performed NNPM on a supercell expanded by a factor of 2 in the  $a$  and  $b$  directions, which we will refer to as the  $2 \times 2 \times 1$  supercell. In this case, 84 water molecules are arranged randomly within a similar fashion as detailed above.

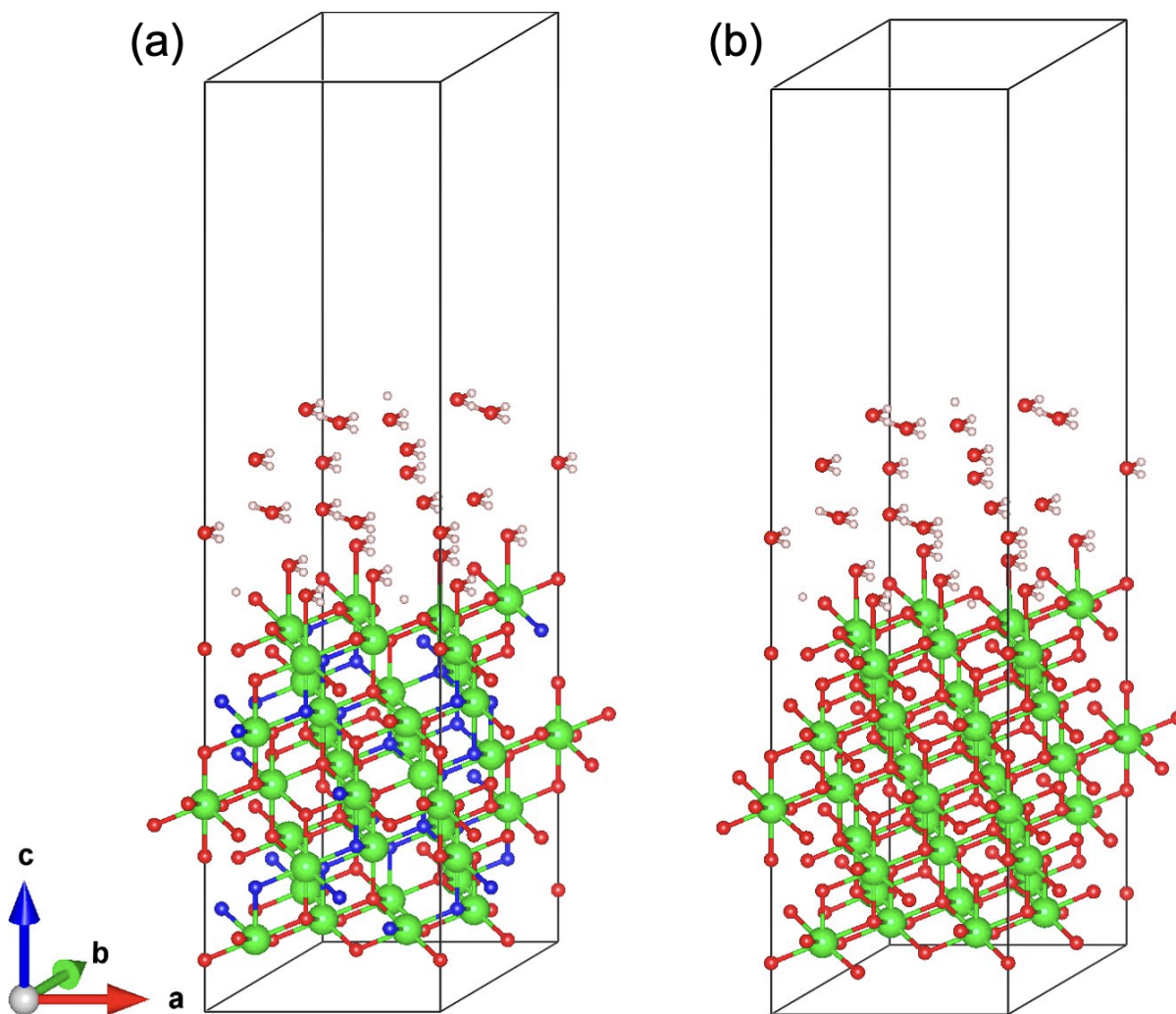


Figure 1: The initial structures of molecular dynamics for interfaces between  $\text{H}_2\text{O}$  and (a)  $\text{Zr}_7\text{O}_8\text{N}_4$  or (b)  $\text{ZrO}_2$ . Green, blue, red and white indicate Zr, N, O and H atoms respectively. The Figures have been generated using the VESTA software package.<sup>42</sup>

## Iterative training of on-lattice neural network model for replica exchange Monte Carlo sampling

## Iterative training of neural network potential for molecular dynamics

Active learning is now recognized as an effective and often necessary procedure for obtaining reliable NNPs in complex systems such as solid/liquid interfaces.<sup>27,30,32,35</sup> In this work, the following active learning procedure was used to generate the NNPs and analyze the structures of adsorbed water:

1. The total energy, interatomic forces, and stress tensor data are obtained for atomic configurations from 4 independent 1 ps AIMD trajectories for the interface model (Fig. 1).
2. An NNP is trained on this data set and used to perform 4 independent 1 ns NNPM D simulations.
3. 400 structures are sampled from the NNPM D trajectories and recalculated using ab initio calculations to obtain the total energy, interatomic forces and stress tensor data. Structures with NNP errors  $\geq 1$  meV/atom are added to the training set.
4. Repeat from 2 until the RMSE of the NNP prediction vs. ab initio calculations in step 3 is smaller than 10 meV/atom.

We then carefully examined the convergence of the resulting NNP model when applied to the  $2 \times 2 \times 1$  expanded supercell. NNPM D was performed for 1 ns in the  $2 \times 2 \times 1$  supercell, then 40 configurations from the NNPM D trajectory was recalculated using ab initio calculations to evaluate the NNP energy errors. If the RMSE  $\geq 10$  meV/atom, we return to the active learning procedure outlined above. After passing this energy error test, we performed 1000 independent NNPM D simulations to calculate average adsorption statistics. In the first pass,

we return to the active learning in the smaller cell for one more iteration. In the subsequent iterations, convergence is examined for the adsorption statistics; if the convergence is judged to be insufficient, we perform additional active learning iterations in the original supercell of Fig. 1. We judge the convergence to be sufficient when the errors are small enough to discuss the difference between the oxide and the oxynitride. The full procedure including details of splitting of training, validation, and test data is outlined in Fig. ??.

The calculation software used for each procedure and the detailed calculation conditions are as follows. *ab initio* calculations were performed using the VASP code,<sup>43,44</sup> which is based on the plane-wave pseudopotential method. Projector augmented wave pseudopotentials<sup>45</sup> and the exchange correlation functional based on the generalised gradient approximation of the Perdew-Burke-Ernzerhof type<sup>46</sup> were used. The projection operator was evaluated in real space, including the non-spherical contribution to the gradient of the density of potential spheres. Only the  $\Gamma$  point was sampled for the Brillouin zone and partial occupancies were calculated by Gaussian smearing with a width of 0.03 eV. The cutoff energy for the plane-wave-basis set is 520 eV. Self-consistent calculations were performed for up to 100 loops and stopped when the energy difference was less than 0.1 meV. The initial magnetic moment was set to  $0.6 \mu_B$  for all atoms to account for spin polarisation. The mass of the hydrogen atoms was replaced by the mass of deuterium, allowing a larger time step in the integration of the equation of motion. AIMD was performed in the NVT ensemble whose temperature was controlled at 300 K by the Langevin thermostat with a friction coefficient of  $10 \text{ ps}^{-1}$ .

The NNPs were generated using SIMPLE-NN (ver. 2),<sup>47,48</sup> which is based on the Behler-Parinello type symmetry function.<sup>40</sup> The parameters of the radial symmetry function  $G_2$  are  $R_{\text{cut}} = 6.0$ ,  $\eta = 0.003214, 0.035711, 0.071421, 0.124987, 0.214264, 0.357106, 0.714213, 1.428426$ ,  $R_s = 0.0$ . Those of the angular symmetry function  $G_3$  are  $R_{\text{cut}} = 6.0$ ,  $\eta = 0.000357, 0.028569, 0.089277$ ,  $\lambda = -1, 1$ ,  $\zeta = 1, 2, 4$ . A neural network is constructed with these symmetry functions as input and the total energy, interatomic forces and stress tensor as output. The neural network contains two hidden layers with 30 nodes each and employs



the tanh activation function. Its weights are optimized up to 1000 epochs using the Adam method with a learning rate of 0.001.

The NNPMMD calculations were performed using LAMMPS.<sup>49,50</sup> The NVT ensemble was used with the temperature controlled to 300 K by the Langevin thermostat with the damping factor of 0.1 ps. The mass of the hydrogen atom was replaced by the mass of the deuterium atom. Four initial structures were created using the method described above, each with a different initial velocity and a 1 ns NNPMMDs was performed for each with a 1 fs time step.

Self-consistent field calculations were performed in VASP for 400 structures every 10 ps in four 1 ns trajectories, and the ab initio and NNP energy errors were checked. Samples with an energy error greater than 1 meV/atom were added to the training and validation data, but not to the test data.

When the energy error was less than 10 meV/atom for both the unit cell and the  $2 \times 2 \times 1$  supercell, the structural properties used for the convergence decision condition of active learning were calculated. For the  $2 \times 2 \times 1$  supercell, 1000 new initial structures were generated and NNPMMD was performed on each of them for 500 ps with a time step of 1 fs. The mean and standard deviation of the number of molecular and dissociative adsorptions were calculated using 1000 structures at 500 ps. The conditions for O adsorption on the Zr site and OH covalent bonds were set to 3.09651 Å and 1.2 Å respectively. When it was determined that these properties had sufficiently converged, active learning was stopped and the other properties - number density distribution for the surface perpendicular and parallel, adsorption distance  $d$ , adsorption angle  $\alpha$ , molecular orientation  $\beta$ , OH orientation  $\gamma$ , number of hydrogen bonds and radial distribution function - were also calculated. Definitions of angles and hydrogen bonds will be explained later. In summary, if the RMSE of the unit cell is below 10 meV/atom, the RMSE of the  $2 \times 2 \times 1$  supercell is calculated; if it is also below 10 meV/atom, the number of adsorptions is calculated; if it converges, active learning is stopped and the other properties are calculated.

## Proton transfer

We calculated the free energy in proton transfer (PT) using different collective variables (CVs). The PT reactions treated in this study are summarised in the Table 1. The CV  $= \delta_{\min}$  was used for PT between donor oxygen  $O_d$  and acceptor oxygen  $O_a$  in hydrogen bonding.<sup>51</sup> This CV is the minimum value of the difference  $\delta$  between the  $O_a$ -H and  $O_d$ -H distances for each time step arrangement of the MD, and used for surface-PT, adlayer-PT, and PT involving solvent 1 to 4 in the Table 1. For the PT between  $O_d$  and  $O_a$  mediated by  $H_2O$ , we used the CV  $= (\delta_1 + \delta_2)/2$ . This CV is the average value of  $\delta_1, \delta_2$  in the hydrogen bond between  $O_d$  or  $O_a$  and the intermediate oxygen  $H_2O$ , and used for solvent-assisted PT in the Table 1. In addition, we used CV  $= S_{O-H}$  for the PT between surface oxygen atoms and any oxygen. This CV is the minimum distance between a given oxygen and any hydrogen on the surface. When using this CV, it is not clear which PT is between the surface oxygen and which oxygen. We calculated the histogram  $W(CV)$  with a bin width of 0.1 Å for each CV and evaluated the Helmholtz free energy  $\Delta F(CV) = -k_B T \ln W(CV)$ . In the free energy calculation, structures at 401,402,...,500 ps were extracted from the 1000 trajectories of the 500 ps MD described above, and a total of 100000 structures were used.

Table 1: The PT reaction formulas and names treated in this study. Adsorbed oxygen, oxygen of the slab surface and oxygen in the solvent are expressed as  $O^*$ ,  $O_s$  and  $O^\sim$  respectively.

$O_s H^-$	$+ O^* H^-$	$\rightleftharpoons$	$O_s^{2-}$	$+ H_2 O^*$	surface-PT		
$H_2 O^*$	$+ O^* H^-$	$\rightleftharpoons$	$O^* H^-$	$+ H_2 O^*$	adlayer-PT		
$O_s H^-$	$+ O^\sim H^-$	$\rightleftharpoons$	$O_s^{2-}$	$+ H_2 O^\sim$	PT involving solvent 1		
$O_s H^-$	$+ H_2 O^\sim$	$\rightleftharpoons$	$O_s^{2-}$	$+ O^\sim H_3^+$	PT involving solvent 2		
$H_2 O^*$	$+ O^\sim H^-$	$\rightleftharpoons$	$O^* H^-$	$+ H_2 O^\sim$	PT involving solvent 3		
$O^* H^-$	$+ O^\sim H_3^+$	$\rightleftharpoons$	$H_2 O^*$	$+ H_2 O^\sim$	PT involving solvent 4		
$O_s H^-$	$+ H_2 O^\sim$	$+ O^* H^-$	$\rightleftharpoons$	$O_s^{2-}$	$+ H_2 O^\sim$	$+ H_2 O^*$	solvent-assisted PT 1
$O_s H^-$	$+ H_2 O^\sim$	$+ O_s^{2-}$	$\rightleftharpoons$	$O_s^{2-}$	$+ H_2 O^\sim$	$+ O_s H^-$	solvent-assisted PT 2
$H_2 O^*$	$+ H_2 O^\sim$	$+ O^* H^-$	$\rightleftharpoons$	$O^* H^-$	$+ H_2 O^\sim$	$+ H_2 O^*$	solvent-assisted PT 3

The lifetime  $\tau$  was evaluated from the time correlation function  $C(t)$  based on the “stable states picture” (SSP).<sup>52</sup> The  $C(t)$  represents the probability that if a molecule is a ”stable” reactant at time  $t_0$ , it is not yet a ”stable” product at time  $t_0 + t$ . The SSP assumes that

an intermediate region exists between stable reactants and stable products. The definition of stable state in PT is as follows:

1. In  $\text{O}^*\text{H}^-$  and  $\text{O}_s\text{H}^-$ , one H atom is coordinated within an oxygen sphere with radius of 1.1 Å, and no other H atom is coordinated within a maximum distance of 1.4 Å.
2. In  $\text{H}_2\text{O}^*$ , two H atoms are coordinated within an oxygen sphere of radius 1.1 Å.
3. In  $\text{O}_s^{2-}$ , H atoms are not coordinated within an oxygen sphere of radius 1.5 Å. In the same way, we also calculated the lifetime of the water adsorption/desorption. In this case, the definition of stable state is as follows.
4. In the adsorbed state, one Zr atom is coordinated within the 2.2 Å radius sphere around the oxygen of the water molecule.
5. In the desorption state, the Zr atom is not coordinated within the 3.2 Å radius sphere around the oxygen of the water molecule.

In order to calculate the time correlation function, 50 ps MD was newly executed using 100 initial structures selected from the 1000 final structures of 500 ps MD described above. We took the average of  $C(t)$  calculated by varying the time origin from 0 to 25 ps, and averaged them over 100 trajectories. We fitted  $C(t)$  with the double exponential function  $A \exp(-t/\tau_1) + (1 - A) \exp(-t/\tau_2)$  and calculate the lifetime as a weighted average  $\tau = A\tau_1 + (1 - A)\tau_2$ , which is equivalent to integrating  $C(t)$  from time zero to infinity.

To investigate the effective long-range diffusion of protons, we calculated the mean squared displacement (MSD) and the diffusion coefficient of the proton hole centers (PHCs).<sup>53</sup> The PHC is defined as a combination of typical acceptors,  $\text{O}_s^{2-}$  and  $\text{O}^*\text{H}^-$ . For this purpose, we performed a new 50 ns MD with an initial structure selected from the 1000 final 500 ps MD structures mentioned above. The MD trajectory were recorded at 100 ps intervals.

To investigate the types of PT that contribute to the long-range diffusion of protons, we have visualised the pathway along which PT occurs. If the oxygen binding to H changes

from  $O_a$  to  $O_b$  at time  $t=i,i+1$ , draw a line segment connecting the coordinates  $O_a(i)$  and  $O_b(i+1)$  at each time and the PT path. In addition, the PT paths were classified according to their oxygen states. In this calculation, we again used the 100 trajectories of 50 ps MD used in the calculation of the time correlation function.

## Anharmonic OH vibrational spectrum

In addition, we have calculated anharmonic OH stretching vibration frequencies based on instantaneous MD simulation snapshots.<sup>24,54,55</sup> For more information on this method, see reference. All anharmonic stretching frequencies were calculated as follows. First, we selected a snapshot of the MD simulation and generated configurations with different O and H coordinates for each OH group contained in it. In these configurations, the centroid coordinates of OH remain unchanged and the distance  $r_{OH}$  (Å) expands and contracts from 0.68 to 1.70 in steps of 0.02. The potential energy of each configuration generated in this way was calculated using the NNP generated by the method described above, and the one-dimensional potential energy  $V(r_{OH})$  was obtained. We fitted  $V(r_{OH})$  with an 11th order polynomial  $V_{11}(r_{OH})$  and expanded it around the minimum equilibrium bond length  $r_{OH}(eq)$ .

$$V_{11}(r_{OH}) = V_0 + \sum_{n=1}^{11} \frac{k_n}{n!} (r_{OH} - r_{OH}(eq))^n \quad (1)$$

The one-dimensional Schrödinger equation for  $V_{11}(r)$  is solved using the discrete variable representation method,<sup>56-58</sup> and the anharmonic OH frequency  $\nu$  is calculated from the energy difference between the ground state and the first excited state. A histogram with a bin width of 100 ( $cm^{-1}$ ) was calculated from the  $\nu$  data set for all oscillators, and the OH vibrational spectral bands were obtained by fitting to an asymmetric Gaussian function.<sup>59</sup>

$$G(\nu) = \frac{A}{\gamma} \sqrt{\frac{4 \ln 2}{\pi}} \exp \left[ -4 \ln 2 \left( \frac{\nu - \nu_{max}}{\gamma} \right)^2 \right] \quad (2)$$

$$\gamma = \frac{2\gamma_0}{1 + \exp[\alpha(\nu - \nu_{max})]} \quad (3)$$

where  $A$  is the peak area,  $\nu$  is the wavenumber frequency,  $\nu_{max}$  is the position of the peak maximum, and  $\gamma_0$  is the full width at half maximum. In the free energy calculation, structures at 500 ps were extracted from the 1000 trajectories of the 500 ps MD described above, and a total of 1000 structures were used.

## Results and discussion

### Validation of NNP

Table 2: The root mean squared error (RMSE) of the existing data set for the total energy, the interatomic force and the stress tensor for the NNP of each loop in  $\text{Zr}_7\text{O}_8\text{N}_4$  and  $\text{ZrO}_2$  for training, validation and test data.

$\text{Zr}_7\text{O}_8\text{N}_4$ loop	Energy (meV/atom)			Force (eV/Å)			Stress (kbar)		
	train	valid	test	train	valid	test	train	valid	test
0	1.119	1.184	1.729	0.088	0.118	0.157	1.752	1.987	2.022
1	1.294	1.521	1.548	0.109	0.133	0.160	2.298	2.263	2.178
2	1.998	1.695	2.347	0.113	0.128	0.148	2.023	1.980	2.103
3	2.122	2.587	2.302	0.133	0.162	0.158	2.144	2.241	2.292
4	1.530	1.866	1.818	0.133	0.141	0.159	2.488	2.558	2.795
$\text{ZrO}_2$ loop	Energy (meV/atom)			Force (eV/Å)			Stress (kbar)		
	train	valid	test	train	valid	test	train	valid	test
0	0.826	0.819	1.061	0.083	0.103	0.130	1.822	1.781	1.938
1	3.865	2.135	2.117	0.137	0.164	0.147	2.866	4.953	1.927
2	3.565	2.088	2.177	0.151	0.163	0.141	3.232	4.531	2.647
3	3.043	4.622	1.826	0.153	0.155	0.150	3.011	3.020	2.092
4	3.267	1.834	1.295	0.151	0.163	0.138	2.919	2.508	1.783

Table 2 shows the root mean squared error (RMSE) for the  $\text{Zr}_7\text{O}_8\text{N}_4$  and  $\text{ZrO}_2$  NNPs against existing data sets. The energy error is less than 10 meV/atom in each loop. In most cases the relative difference between loops is less than 10%. Although the NNP appears to converge sufficiently without going to loop 4, the NNP accuracy should not be judged solely on the basis of the RMSEs of the existing data. This is because, as discussed below, the RMSEs of the newly acquired data in the molecular dynamics trajectories performed with these NNPs are not necessarily 10 meV/atom.

Table 3: RMSE in the total energy of the newly acquired data, which are included in the NNPM trajectory of  $\text{Zr}_7\text{O}_8\text{N}_4$  and  $\text{ZrO}_2$ . For loops 0 and 1, RMSEs for  $2 \times 2 \times 1$  supercells were not calculated due to large RMSEs for unit cell and the non-convergence for self-consistent calculation, respectively.

$\text{Zr}_7\text{O}_8\text{N}_4$		unit cell				$2 \times 2 \times 1$ supercell			
loop	run = 1	2	3	4	run = 1	2	3	4	
0	10.572	17.765	11.313	10.633					
1	4.833	7.105	5.323	5.113					
2	2.317	2.140	8.145	2.143	2.279	2.353	5.398	2.299	
3	1.626	1.541	1.603	1.442	1.931	6.112	6.553	6.647	
4	1.202	1.178	1.392	1.384	1.310	1.199	1.428	1.345	
$\text{ZrO}_2$		unit cell				$2 \times 2 \times 1$ supercell			
loop	run = 1	2	3	4	run = 1	2	3	4	
0	28.576	28.416	28.955	25.323					
1	1.900	1.939	1.899	2.100					
2	1.628	2.553	1.514	1.573	6.632	6.231	5.308	5.153	
3	1.469	1.094	1.088	1.152	4.936	5.024	5.159	5.116	
4	2.644	1.160	1.625	2.123	3.021	3.902	3.884	3.543	

Table 3 shows the errors in the ab initio self-consistent calculations for the structures included in the NNPM trajectory of  $\text{Zr}_7\text{O}_8\text{N}_4$  and  $\text{ZrO}_2$ . Ab initio self-consistent calculations were also performed for  $2 \times 2 \times 1$  supercells only in loops 1-4, where the RMSE in the unit cell is less than 10 meV/atom. In loop 1, the RMSEs and structural properties were not calculated because the self-consistent calculations of  $2 \times 2 \times 1$  supercells did not converge for some structures. The RMSEs of loops 2, 3, and 4 were  $< 10$  meV/atom in both cells, so structural properties were calculated. Note that the total energies in 1 ns NNPMs reach equilibrium after about 0.1 ns and are conserved without significant increase or decrease thereafter.

Whether sufficient time and the number of trajectories were used to calculate the structural properties was verified by the number of adsorptions calculated from the loop 4 NNPM trajectory of  $\text{Zr}_7\text{O}_8\text{N}_4$ . Figure 2 (a) shows the time dependence of the number of adsorptions calculated from the 10, 20, ..., 500 ps structure of 1000 trajectories. It can be seen that it converges to 0.1 at 400 ps. Figure 2 (b) shows the dependence of the number of adsorptions on the number of trajectories calculated from the 500 ps structure of 2, 3, ...,

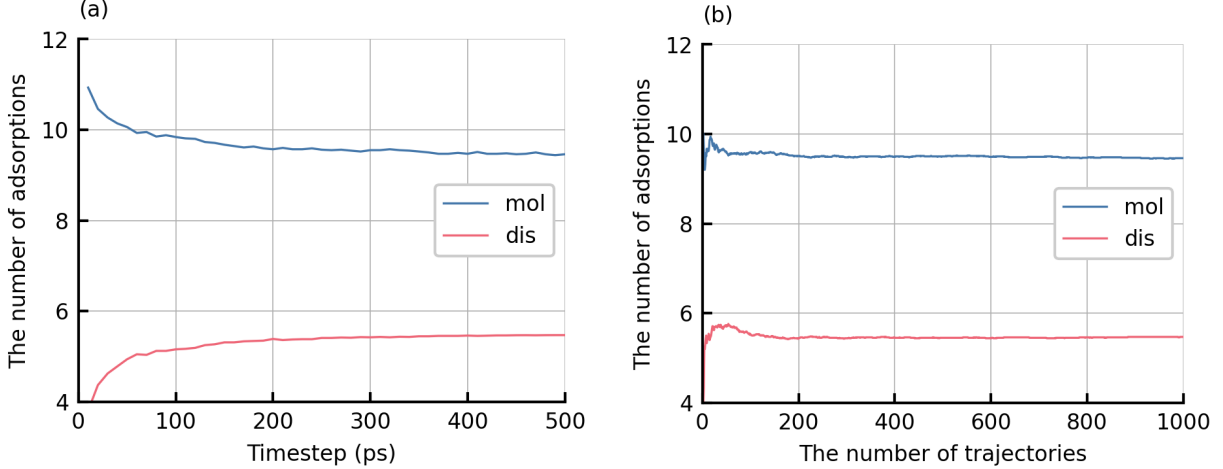


Figure 2: Dependence of the number of adsorptions on (a) timestep and (b) the number of trajectories. Blue and red represent molecular (mol) and dissociative (dis) adsorption, respectively. These were calculated from loop 4 NNPMO trajectories of  $\text{Zr}_7\text{O}_8\text{N}_4$ .

1000 trajectories. It can be seen that the number converges to 0.1 for 200 trajectories. Thus the number of adsorptions calculated from the 500 ps structure of 1000 trajectories can be trusted to the order of 0.1.

Table 4: Mean values of the number of molecular (mol) and dissociative (dis) adsorptions in  $\text{Zr}_7\text{O}_8\text{N}_4$  and  $\text{ZrO}_2$ . The values in brackets are standard deviations. For both materials, these were calculated from loop 2, 3 and 4 NNPMO trajectories.  $N$  = the number of adsorptions in a  $2 \times 2 \times 1$  supercell.  $M = N/4$  = the number of adsorptions per unit cell.  $C$  = coverage (%) =  $N/28$  (= the number of Zr sites in  $2 \times 2 \times 1$  supercell surface)\*100.

$\text{Zr}_7\text{O}_8\text{N}_4$						
loop	$N_{\text{mol}}$	$N_{\text{dis}}$	$M_{\text{mol}}$	$M_{\text{dis}}$	$C_{\text{mol}}$	$C_{\text{dis}}$
2	9.6 (1.2)	5.8 (1.1)	2.4 (0.3)	1.5 (0.3)	34 (4)	21 (4)
3	10.2 (1.2)	5.5 (1.0)	2.5 (0.3)	1.4 (0.2)	36 (4)	20 (3)
4	9.5 (1.1)	5.5 (1.0)	2.4 (0.3)	1.4 (0.3)	34 (4)	20 (4)
$\text{ZrO}_2$						
loop	$N_{\text{mol}}$	$N_{\text{dis}}$	$M_{\text{mol}}$	$M_{\text{dis}}$	$C_{\text{mol}}$	$C_{\text{dis}}$
2	4.1 (1.4)	9.3 (1.3)	1.0 (0.4)	2.3 (0.3)	15 (5)	33 (5)
3	6.2 (1.4)	9.1 (1.2)	1.6 (0.4)	2.3 (0.3)	22 (5)	33 (4)
4	5.6 (1.4)	9.6 (1.2)	1.4 (0.4)	2.4 (0.3)	20 (5)	34 (4)

Table 4 shows the number of molecular and dissociative adsorptions ( $N$ ) of  $\text{Zr}_7\text{O}_8\text{N}_4$  and  $\text{ZrO}_2$  calculated by each loop NNP. For reference, the number of adsorptions per unit cell ( $M$ ), converted from the number of adsorptions per  $2 \times 2 \times 1$  supercell, and the coverage

(C) are also given. For the number of adsorptions  $N$ , the mean difference between loops 3 and 4 is up to 0.7 and the standard deviation between the materials is up to 2.5. Both are small compared to the difference between materials in loop 4, 2.9, so we consider that the convergence is not a problem for comparing these materials.

## Structural analysis

The relationship between the number of molecular and dissociative adsorptions is reversed between  $\text{Zr}_7\text{O}_8\text{N}_4$  and  $\text{ZrO}_2$ . Because  $\text{Zr}_7\text{O}_8\text{N}_4$  has less oxygen for the  $\text{V}_\text{O}$ , the dissociated excess  $\text{H}^+$  is less likely to be adsorbed on oxygen and more likely to re-bind to dissociatively adsorbed  $\text{OH}^-$ , which is the cause. This idea is also supported by the fact that the total number of adsorptions is almost the same for  $\text{Zr}_7\text{O}_8\text{N}_4$  and  $\text{ZrO}_2$ . In addition,  $\text{Zr}_7\text{O}_8\text{N}_4$  is charge neutral due to the presence of the  $\text{V}_\text{O}$  and  $\text{N}_\text{O}$  defects, so it is unlikely that the  $\text{V}_\text{O}$  is responsible for attracting the O atom. According to a study by Muhammady et al.,<sup>18</sup> where one  $\text{V}_\text{O}$  and two  $\text{N}_\text{O}$  defects were introduced into the tetragonal- $\text{ZrO}_2$  (101) surface, the  $\text{V}_\text{O}$  is not more easily adsorbed by the  $\text{O}_2$  molecule than the Zr atom. Therefore, it is consistent with the present results to consider that the  $\text{V}_\text{O}$  does not promote dissociation by accepting the O of water molecules. The dissociative adsorption becomes molecular adsorption, which reduces the probability that intermediates and the  $\text{H}^+$  that binds to them in the ORR will have an additional reaction with nearby adsorbates, i.e. the ORR is more likely to proceed in the presence of oxygen defects. Also, while the total number of adsorptions is almost the same and the number of vacant Zr sites is almost the same,  $\text{Zr}_7\text{O}_8\text{N}_4$  has two  $\text{V}_\text{O}$ s per unit cell, which could also be an active site for the ORR. In other words,  $\text{Zr}_7\text{O}_8\text{N}_4$  has more active sites and is more likely to promote the ORR than  $\text{ZrO}_2$ .

Figure 3 shows the surface perpendicular number density distributions of  $\text{Zr}_7\text{O}_8\text{N}_4$  and  $\text{ZrO}_2$ . The densities of total, oxygen and hydrogen atoms in water at the interface and hydrogen atoms in bulk water are shown respectively. The surface perpendicular number density distribution shows that the oxygen peak in the adsorption layer (16-18 Å) is one in



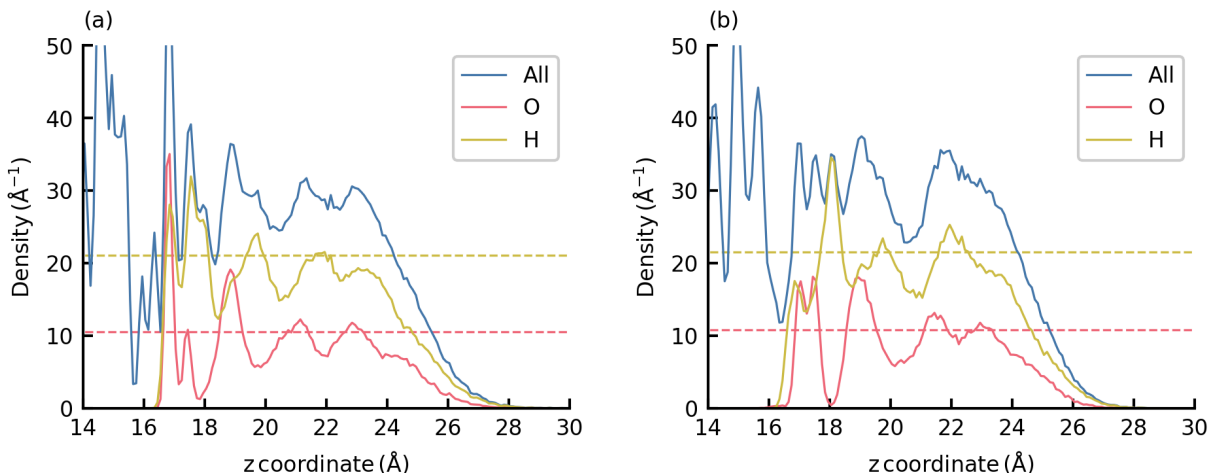


Figure 3: Surface perpendicular number density distributions ( $\text{\AA}^{-1}$ ) of (a)  $\text{Zr}_7\text{O}_8\text{N}_4$  and (b)  $\text{ZrO}_2$ . The blue, red and yellow solid lines represent total, oxygen and hydrogen atoms in water at the interface. The red and yellow dashed lines represent oxygen and hydrogen atoms in bulk water. These densities for both materials were calculated from loop 4 NNPM trajectories.

$\text{ZrO}_2$ , whereas it is divided into two in  $\text{Zr}_7\text{O}_8\text{N}_4$ , which is due to the fact that the height of the Zr sites is almost the same in all  $\text{ZrO}_2$  and is divided into two types in  $\text{Zr}_7\text{O}_8\text{N}_4$ . Differences in the surface-derived adsorption structures will affect their function as catalysts for the ORR, as well as the diffusion of molecules and protons.

Away from the surface, the number density oscillates and is not constant as in the bulk. In other words, the motion is limited compared to the bulk. According to a previous study of the  $\text{Cu}/\text{H}_2\text{O}$  interface,<sup>21</sup> water molecules move like the bulk when the thickness of their layer is more than  $30 \text{\AA}$ . In the present study, the thickness of the water molecule layer is less than  $15 \text{\AA}$ , which is consistent with the results that it is not constant like the bulk.

Figure 4 shows the surface parallel number density distributions of  $\text{Zr}_7\text{O}_8\text{N}_4$  and  $\text{ZrO}_2$ . Only the densities of the oxygen atoms in the  $\text{H}_2\text{O}$  or  $\text{OH}^-$  adsorbed on the Zr sites are shown. The distribution of  $\text{ZrO}_2$  is uniform and translational symmetry is observed. As mentioned above, this is not due to the initial structure, as the translational symmetry of water is not guaranteed.  $\text{ZrO}_2$  was assumed to have a uniform adsorption distribution due to the equivalent Zr sites on its surface. However, if the adsorption distribution does not

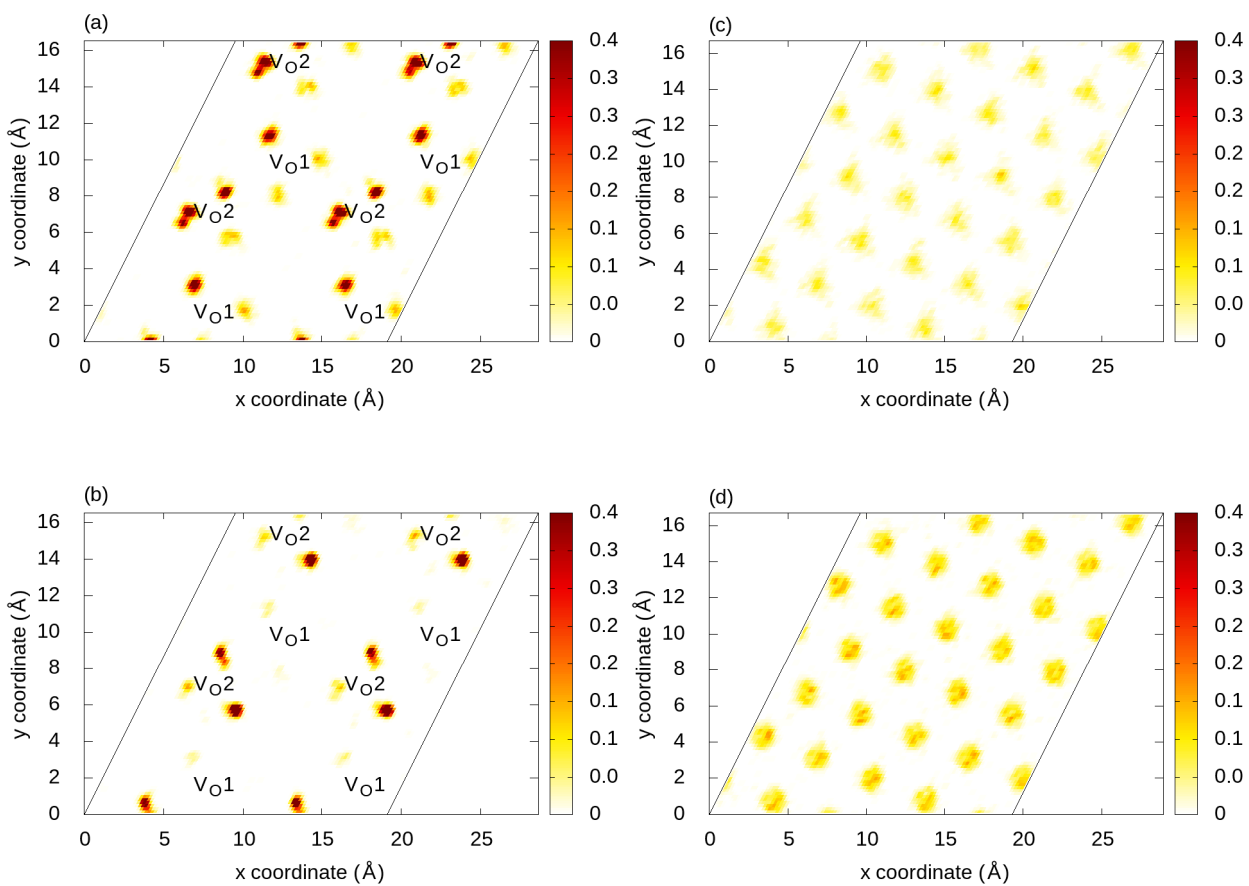


Figure 4: Surface parallel number density distributions ( $\text{\AA}^{-3}$ ) of O atoms in molecular (top) and dissociative adsorption (bottom) in  $Zr_7O_8N_4$  (left) and  $ZrO_2$  (right). Two types of oxygen vacancies in a  $Zr_7O_8N_4$  unit cell are represented by  $V_{O1}$  and  $V_{O2}$ .

change much in 500 ps MD, the adsorption distribution calculated from only one trajectory may not be uniform. In the present study, the adsorption distribution was calculated from 1000 independent trajectories, so that a uniform distribution was obtained, regardless of whether the adsorption distribution was likely to change in 500 ps MD. The distribution of  $\text{Zr}_7\text{O}_8\text{N}_4$  is non-uniform, but translational symmetry is established. This is also a result of obtaining a sufficiently large number of trajectories, rather than the initial structure, and is due to the low computational cost of NNPM, which allows so many MDs to be performed.

Particles were found to adsorb on the Zr, but not on the  $\text{V}_\text{O}$ . Zr atoms around  $\text{V}_\text{O} 2$  are more likely to adsorb particles than those around  $\text{V}_\text{O} 1$ . These results suggest that the  $\text{V}_\text{O}$  act as active sites for the ORR and that differences in adsorption around them affect their function. In particular, we suggest that the  $\text{V}_\text{O} 1$  is more likely to adsorb  $\text{O}_2$  molecules as there is less adsorption on the surrounding Zr atoms.

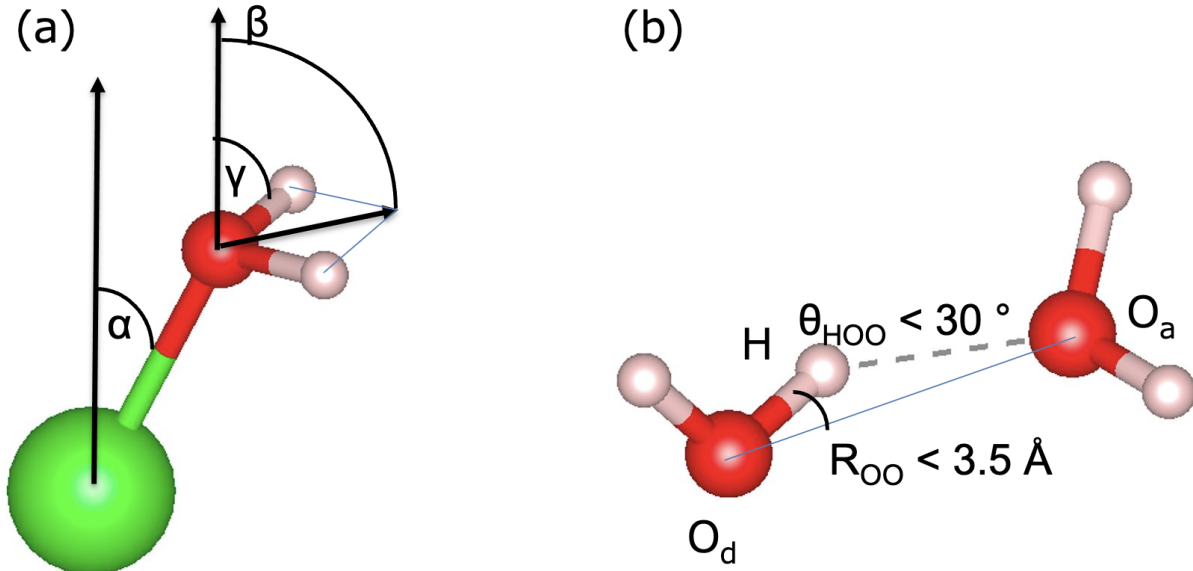


Figure 5: (a) Definition of adsorption angle  $\alpha$ , molecular orientation  $\beta$  and OH orientation  $\gamma$ . (b) Definition of hydrogen bonding. Oxygens donating and accepting hydrogen are denoted  $\text{O}_d$  and  $\text{O}_a$ . Green, red and white indicate Zr, O and H atoms respectively. The Figures have been generated using the VESTA software package.

For other properties, (adsorption distance  $d$ , adsorption angle  $\alpha$ , molecular orientation  $\beta$ , OH orientation  $\gamma$ , and number of hydrogen bonds  $N_{\text{HB}}$ ) their definitions are given before the

Table 5: Adsorption distance  $d$  (Å), adsorption angle  $\alpha$ , molecular orientation  $\beta$ , OH orientation  $\gamma$  and number of hydrogen bonds  $N_{\text{HB}}$  for  $\text{Zr}_7\text{O}_8\text{N}_4$  and  $\text{ZrO}_2$ , for molecular (mol) and dissociative (dis) adsorption.

	$d_{\text{mol}}$	$d_{\text{dis}}$	$\alpha_{\text{mol}}$	$\alpha_{\text{dis}}$	$\beta_{\text{mol}}$	$\gamma_{\text{mol}}$	$\gamma_{\text{dis}}$	$N_{\text{HB}}$
$\text{Zr}_7\text{O}_8\text{N}_4$	2.39	2.20	18.28	17.74	51.68	68.40	53.35	68.70
$\text{ZrO}_2$	2.29	2.11	12.81	20.23	35.03	62.14	62.38	67.56

results are presented. Figure 5 (a) shows the definition of the adsorption angle  $\alpha$ , molecular orientation  $\beta$  and OH orientation  $\gamma$ . The adsorption angle  $\alpha$  is the angle between the position vector of O with respect to Zr and the surface normal. The adsorption distance  $d$  is the absolute value of the vector. The water molecule orientation  $\beta$  is the angle between the dipole vector of the water molecule and the surface normal. The OH orientation  $\gamma$  is the angle between the position vector of H with respect to O and the surface normal. Figure 5 (b) shows the definition of a hydrogen bond. A hydrogen bond is defined when the angle  $\text{H-O}_d\text{-O}_a$  is less than  $30^\circ$ , the distance  $\text{O}_d\text{-H}$  is less than  $1.2 \text{ \AA}$  and the distance  $\text{O}_d\text{-O}_a$  is less than  $3.5 \text{ \AA}$ , where  $\text{O}_d$  and  $\text{O}_a$  are the oxygen donating and accepting hydrogen, respectively.<sup>60</sup>

Table 5 shows the adsorption distance  $d$ , adsorption angle  $\alpha$ , molecular orientation  $\beta$ , OH orientation  $\gamma$ , and the number of hydrogen bonds  $N_{\text{HB}}$  calculated based on the above definition. The adsorption distance  $d$  of  $\text{ZrO}_2$  is  $0.1 \text{ \AA}$  shorter in both molecular and dissociation. The increase or decrease of the adsorption angle  $\alpha$  is opposite for molecular and dissociation, with the adsorption angles becoming unequal, whereas for  $\text{Zr}_7\text{O}_8\text{N}_4$  they were almost equal at  $18^\circ$ . The molecular orientation  $\beta$  of  $\text{ZrO}_2$  decreases, i.e. it turns upwards. The increase and decrease of the OH orientation  $\gamma$  is opposite in molecular and dissociation, going from unequal in  $\text{Zr}_7\text{O}_8\text{N}_4$  to aligned at almost  $62^\circ$ . The number of hydrogen bonds in  $\text{ZrO}_2$  is reduced by one. We consider this to be the effect of a distortion in the distribution of water molecules due to the defect.

Figure 6 shows the Radial Distribution Function (RDF). The oxygens in the slab and in the water is distinguished as  $\text{O}_s$  and  $\text{O}_w$ . Compared to  $\text{ZrO}_2$ , the RDF of  $\text{Zr-O}_w$  in  $\text{Zr}_7\text{O}_8\text{N}_4$  has a lower peak at  $2.1 \text{ \AA}$  and is shifted to the right. This means that the average adsorption

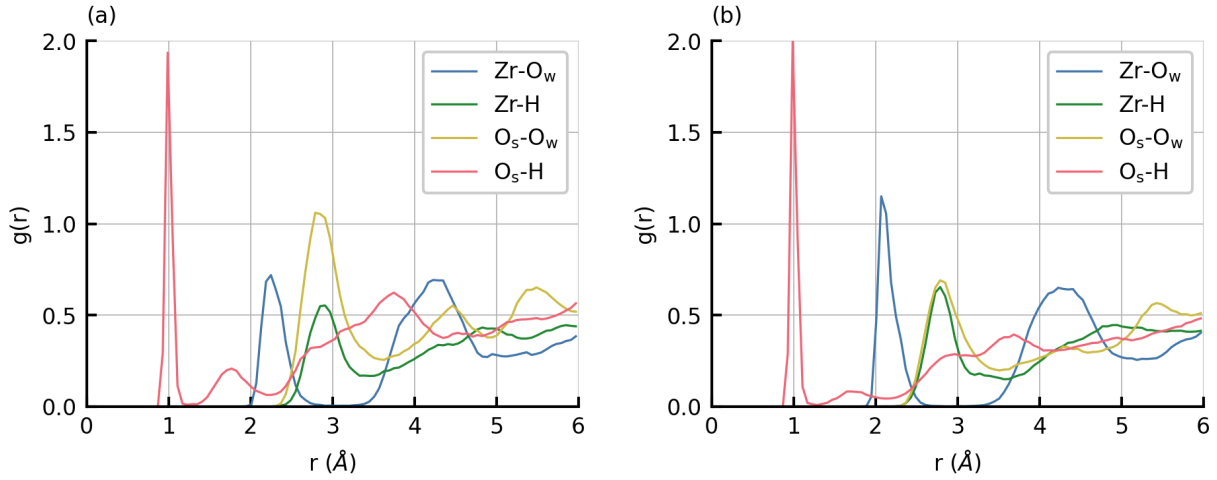


Figure 6: Radial distribution function  $g(r)$  of (a)  $Zr_7O_8N_4$  and (b)  $ZrO_2$ .  $O_s$  and  $O_w$  represent oxygen in the slab and in the water molecule. Blue, green, yellow and red represent Zr- $O_w$ , Zr-H,  $O_s$ - $O_w$  and  $O_s$ -H, respectively.

distance increases. Both molecular and dissociative adsorption distances are shorter for  $Zr_7O_8N_4$ , but the increase in the proportion of molecular adsorption at longer adsorption distances is thought to be the cause. The lower peak at 1 Å in the  $O_s$ -H RDF of  $Zr_7O_8N_4$  is thought to be due to a decrease in H adsorbed on  $O_s$  as dissociative adsorption decreases.

## Proton transfer

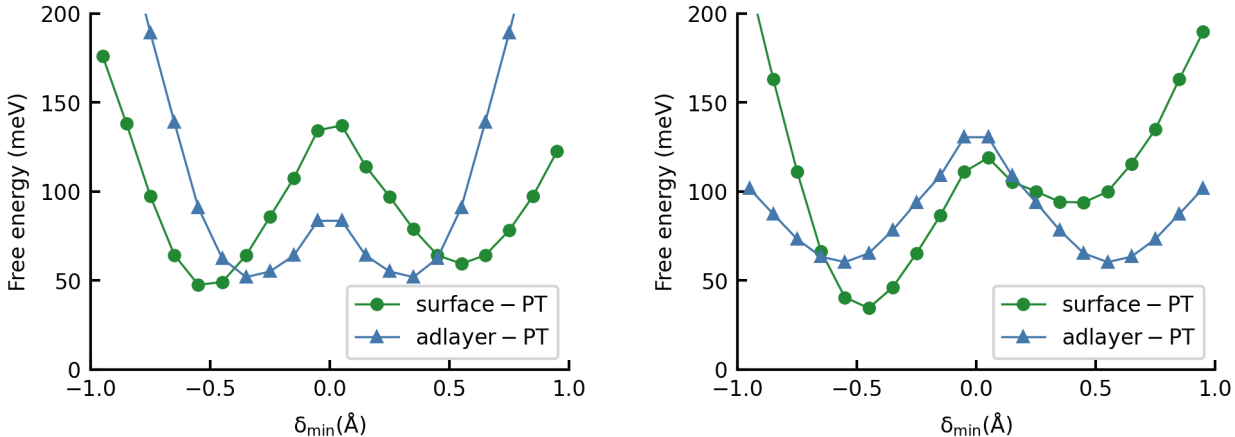


Figure 7: Free energy for  $CV = \delta_{min}$  of surface-PT and adlayer-PT in  $Zr_7O_8N_4$  (left) and  $ZrO_2$  (right). The PT reaction formulas are summarised in the Table 1.

Table 6: Free energy barrier for surface-PT and adlayer PT reaction in  $Zr_7O_8N_4$  and  $ZrO_2$ . The PT reaction formulas are summarised in the Table 1.

	surface-PT		adlayer-PT	
	$\rightarrow$	$\leftarrow$	$\rightarrow$	$\leftarrow$
$Zr_7O_8N_4$	89	78	34	34
$ZrO_2$	89	25	71	71

Figure 7 represents the free energy of the surface PT and the adlayer PT. The surface PT is the PT between adsorbed  $H_2O$  and surface oxygen, The adlayer PT is the PT between adsorbed  $H_2O$  and adsorbed  $OH^-$ . Table 6 shows the barriers in these free energy. The leftward barrier at the surface-PT represents the ease with which molecular adsorption turns into dissociative adsorption, and  $ZrO_2$  has a much lower barrier than  $Zr_7O_8N_4$ . This is consistent with the fact that the number of dissociative adsorptions of  $Zr_7O_8N_4$  is smaller than that of  $ZrO_2$ , as mentioned above. As  $Zr_7O_8N_4$  has less  $O_s$ , adsorption of H onto  $O_s$  is less likely to occur than on  $ZrO_2$ . The barrier in the adlayer PT is lower for  $Zr_7O_8N_4$  than for  $ZrO_2$ . This is thought to be because in  $Zr_7O_8N_4$  the adsorbates in Zr collect around  $V_O$ , so there is a high probability that  $H_2O^*$  and  $O^*H^-$  are adjacent. However, the fact that PT is more likely to occur in  $Zr_7O_8N_4$  does not necessarily mean that protons are more likely to

diffuse over long distances. In  $\text{Zr}_7\text{O}_8\text{N}_4$  the adsorbates tend to be densely packed and even if an adlayer PT frequently occurs between them, protons will circulate in the same place and will not contribute to effective diffusion. We will discuss later how easy it is for protons to actually diffuse over long distances by calculating mean squared displacement and diffusion coefficient.

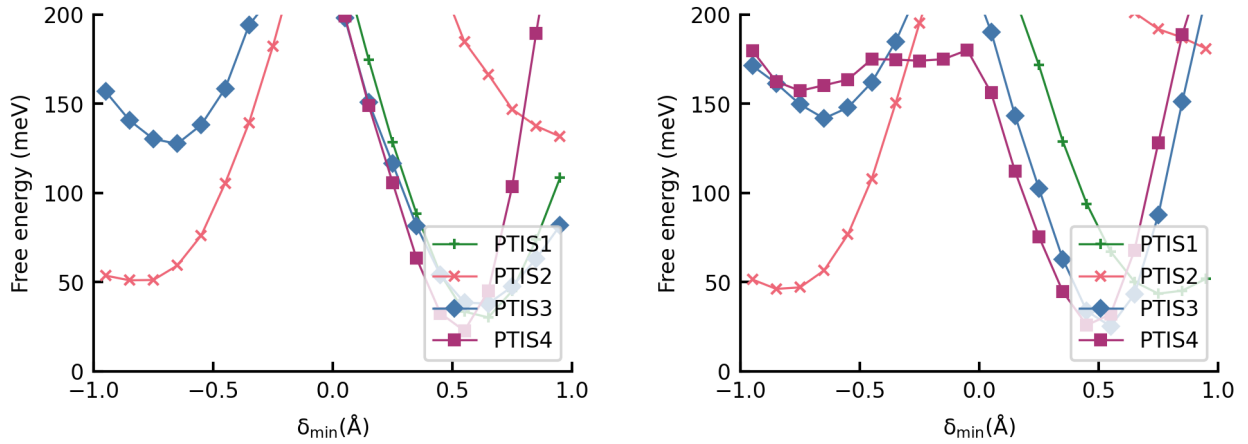


Figure 8: Free energy for  $\text{CV} = \delta_{\min}$  of PT involving the solvent (PTIS) in  $\text{Zr}_7\text{O}_8\text{N}_4$  (left) and  $\text{ZrO}_2$  (right). The PT reaction formulas are summarised in the Table 1.

Figure 8 shows the free energy for  $\text{CV} = \delta_{\min}$  of PT involving the solvent (PTIS). For most PTs the barrier is so high that there is almost no chance of a reaction taking place. Only PTIS4 of  $\text{ZrO}_2$  has a relatively low barrier and a reaction can occur in rare cases.



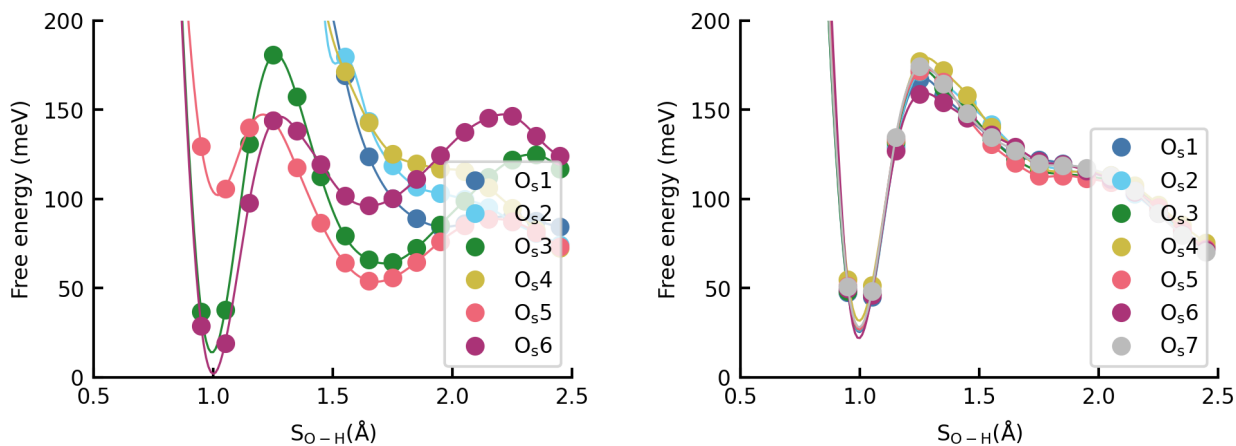


Figure 9: Free energy for  $CV = S_{O-H}$  of PT involving on each  $O_s$  in  $Zr_7O_8N_4$  (left) and  $ZrO_2$  (right). Positions of each  $O_s$  sites is shown in Figure 10.

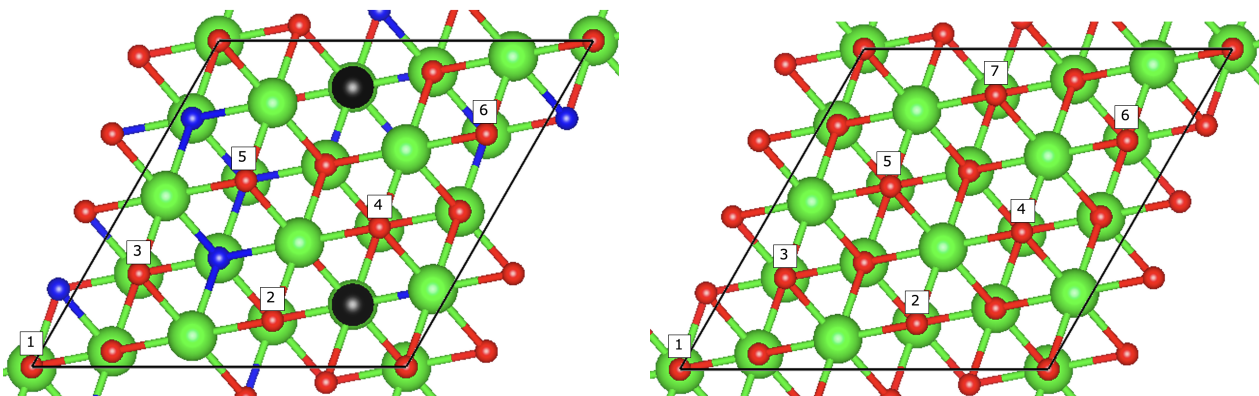


Figure 10: Positions of each  $O_s$  sites in  $Zr_7O_8N_4$  (left) and  $ZrO_2$  (right). Green, blue, red and black indicate Zr, N, O and  $V_O$  respectively. The Figures have been generated using the VESTA software package.

Figure 9 shows the free energy for  $CV = S_{O-H}$  of PT involving on each  $O_s$ . Figure 10 shows the positions of the  $O_s$ s in the collective variable by number. In  $Zr_7O_8N_4$ , since the O atoms on the surface are not equivalent, the free energy differs depending on the  $O_s$ . For  $O_s=1,2,4$ , the  $S_{O-H}$  does not reach a minimum close to 1 and there is no surface PT. The fact that dissociation PT is unlikely to occur in these oxygens near  $V_{O1}$  is consistent with the fact that there is almost no dissociated adsorption density near  $V_{O1}$  (Figure 4). On the other hand, in  $ZrO_2$ , all  $O_s$ s are equivalent, so the free energy is the same for all  $O_s$ s. In any case, with this CV, it is unclear between  $O_s$  and which oxygen (adsorbate or solvent) PT

has occurred.

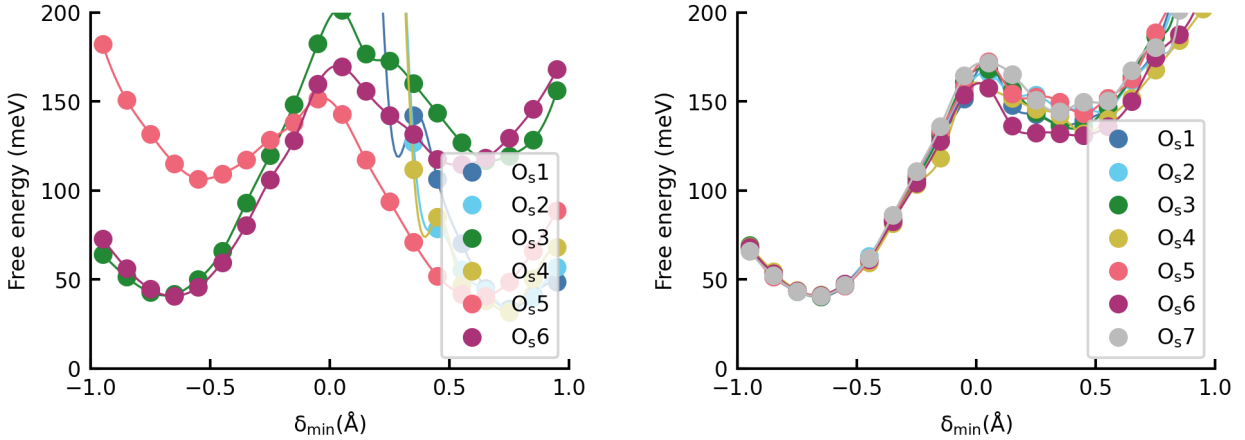


Figure 11: Free energy for  $\text{CV} = \delta_{\min}$  of surface-PT on each  $\text{O}_s$  in  $\text{Zr}_7\text{O}_8\text{N}_4$  (left) and  $\text{ZrO}_2$  (right). Positions of each  $\text{O}_s$  sites is shown in Figure 10. The PT reaction formulas are summarised in the Table 1.

Figure 11 shows free energy for  $\text{CV} = \delta_{\min}$  of surface-PT on each  $\text{O}_s$ . Figure 10 shows the positions of  $\text{O}_s$ s in the collective variable by number. In  $\text{Zr}_7\text{O}_8\text{N}_4$ , since the  $\text{O}_s$ s are not equivalent, the free energy differs depending on the  $\text{O}_s$ . When  $\text{O}_s=1,2,4$ , the free energy becomes infinite in the negative region of  $\delta_{\min}$ , so it can be seen that dissociative adsorption does not occur. On the other hand, in  $\text{ZrO}_2$ , all  $\text{O}_s$ s are equivalent, so the free energy is the same for all  $\text{O}_s$ s. Contrary to Figure 9, it is clear that this collective variable represents a surface-PT between  $\text{O}_s$  and adsorbed water.

Figure 12 represents free energy for  $\text{CV} = S_{\text{O-H}}$  of PT involving all  $\text{O}_s$  sites. Figure 7 While the  $S_{\text{O-H}}$  in Figure 9 is the minimum distance between a "specific"  $\text{O}_s$  and all Hs, this  $S_{\text{O-H}}$  is the minimum distance between "all"  $\text{O}_s$ s and all Hs. In other words, if even one H is adsorbed among all  $\text{O}_s$ , the minimum distance between that adsorbed  $\text{O}_s$  and H is the  $S_{\text{O-H}}$ . Even if H moves from another  $\text{O}_s$ ,  $S_{\text{O-H}}$  does not represent the distance between that the O and the H. Therefore the free energy of the surface PT as shown in Figure 12 cannot be determined from this CV.

The CVs such as those shown in Figures 11 and 12 are not usually used. We were

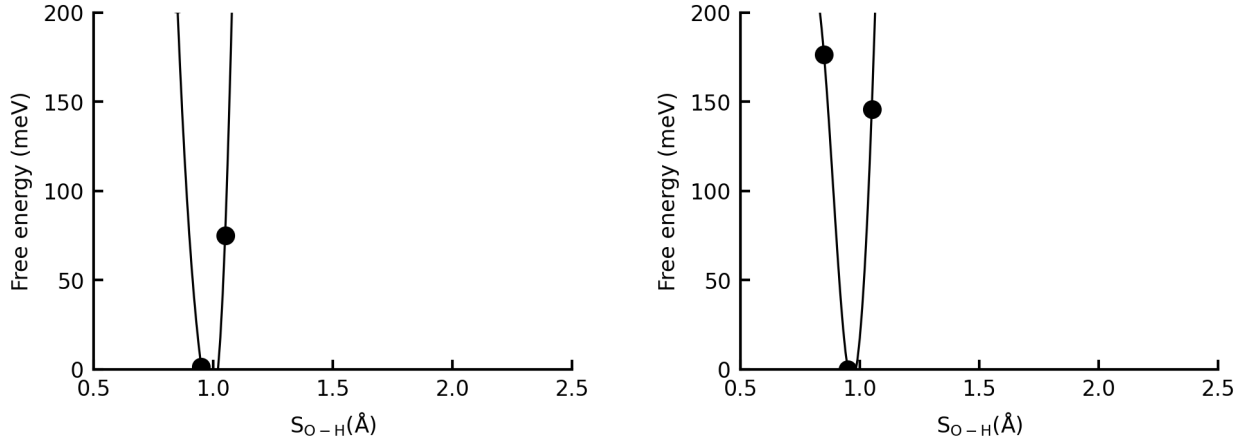


Figure 12: Free energy for  $CV = S_{O-H}$  of PT involving all  $O_s$  sites in  $Zr_7O_8N_4$  (left) and  $ZrO_2$  (right).

interested in whether it would be possible to say which CV is most appropriate, since the free energy barrier seems to be calculated differently depending on how the CV is taken. We carried out calculations using such CVs. This is a different matter from the exact calculation of the free energy surface, and the idea is to compare different CVs and the barriers. We believe that it is not obvious which CVs are important, and that all of CVs seem to be important. Therefore, the free energy for such CVs is also included.

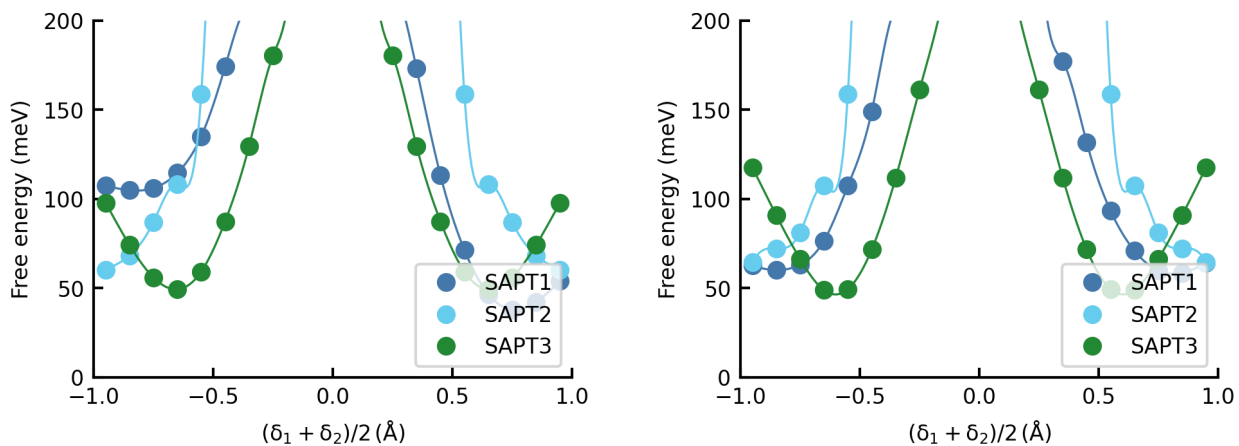


Figure 13: Free energy for  $CV = (\delta_1 + \delta_2)/2$  of solvent-assisted PT (SAPT) in  $Zr_7O_8N_4$  (left) and  $ZrO_2$  (right). The PT reaction formulas are summarised in the Table 1.

Figure 13 represents the free energy of solvent-assisted PT. The PT reactions treated in this study are summarised in the Table 1. All of these PTs have very high free energy barriers, so their probability is quite low.

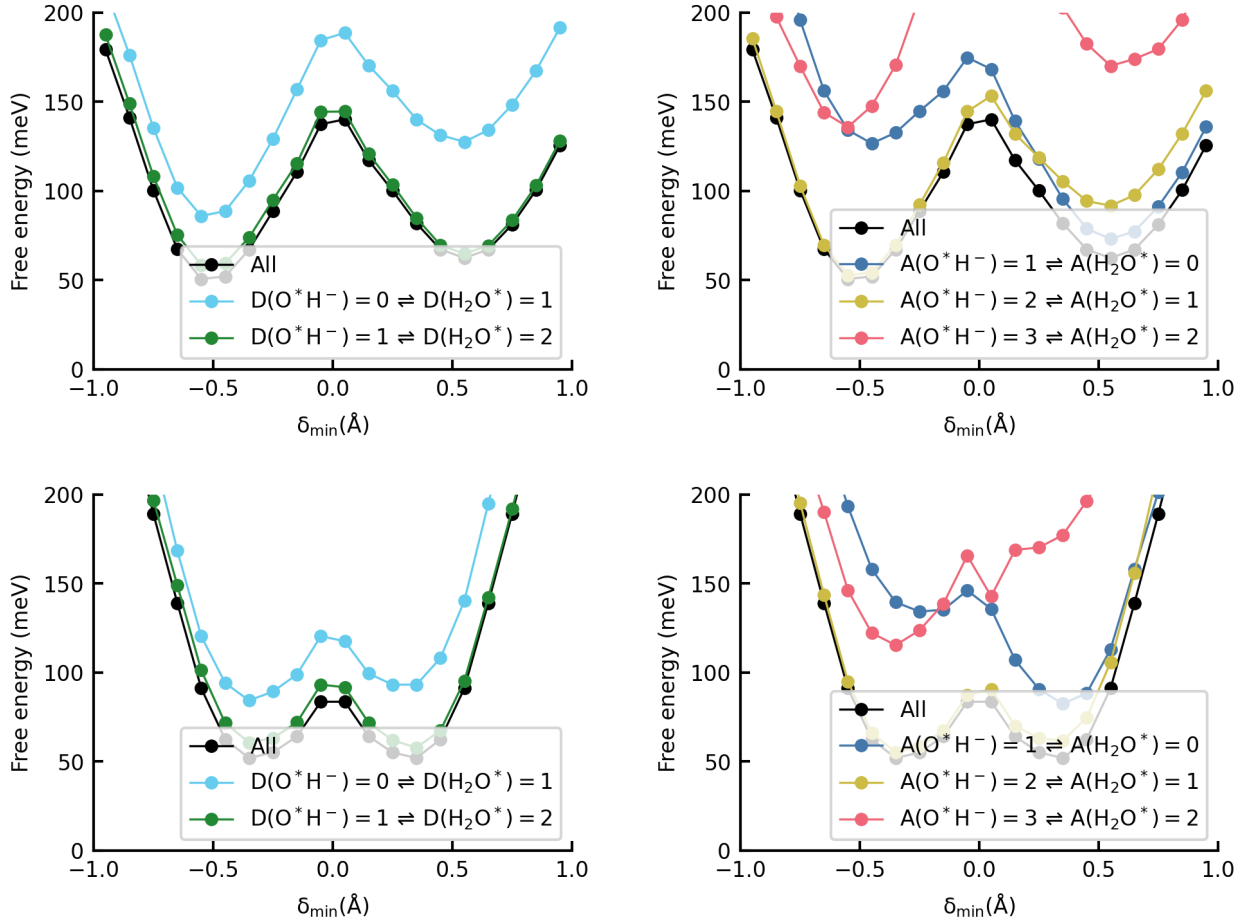


Figure 14: Free energy for  $CV = \delta_{\min}$  of surface-PT (top) and adlayer-PT (bottom) for the number of hydrogen bonds, where  $O^*H^-$  in left-hand side ( $H_2O^*$  in right-hand side) is the donor (D) or acceptor (A) in  $Zr_7O_8N_4$ . The PT reaction formulas are summarised in the Table 1.

Figure 14 shows free energy for  $CV = \delta_{\min}$  of surface-PT and adlayer-PT for the number of hydrogen bonds, where  $O^*H^-$  in left-hand side ( $H_2O^*$  in right-hand side) is the donor or acceptor in  $Zr_7O_8N_4$ . For the surface PT, the free energy curves cross at  $A(H_2O^*)=0,1$ , as in previous studies on  $ZnO$ .<sup>23</sup> In other words, it can be said that there is a predominant pre-solvation mechanism. This means that the most stable value is  $A=0$ , the number at which  $H_2O^*$  accepts hydrogen bonds, but if it increases to  $A=1$  due to thermal fluctuations, the energy barrier decreases and proton transfer becomes more likely. On the other hand, in the adlayer-PT, in contrast to the previous studies on  $ZnO$ , there is no such crossing.

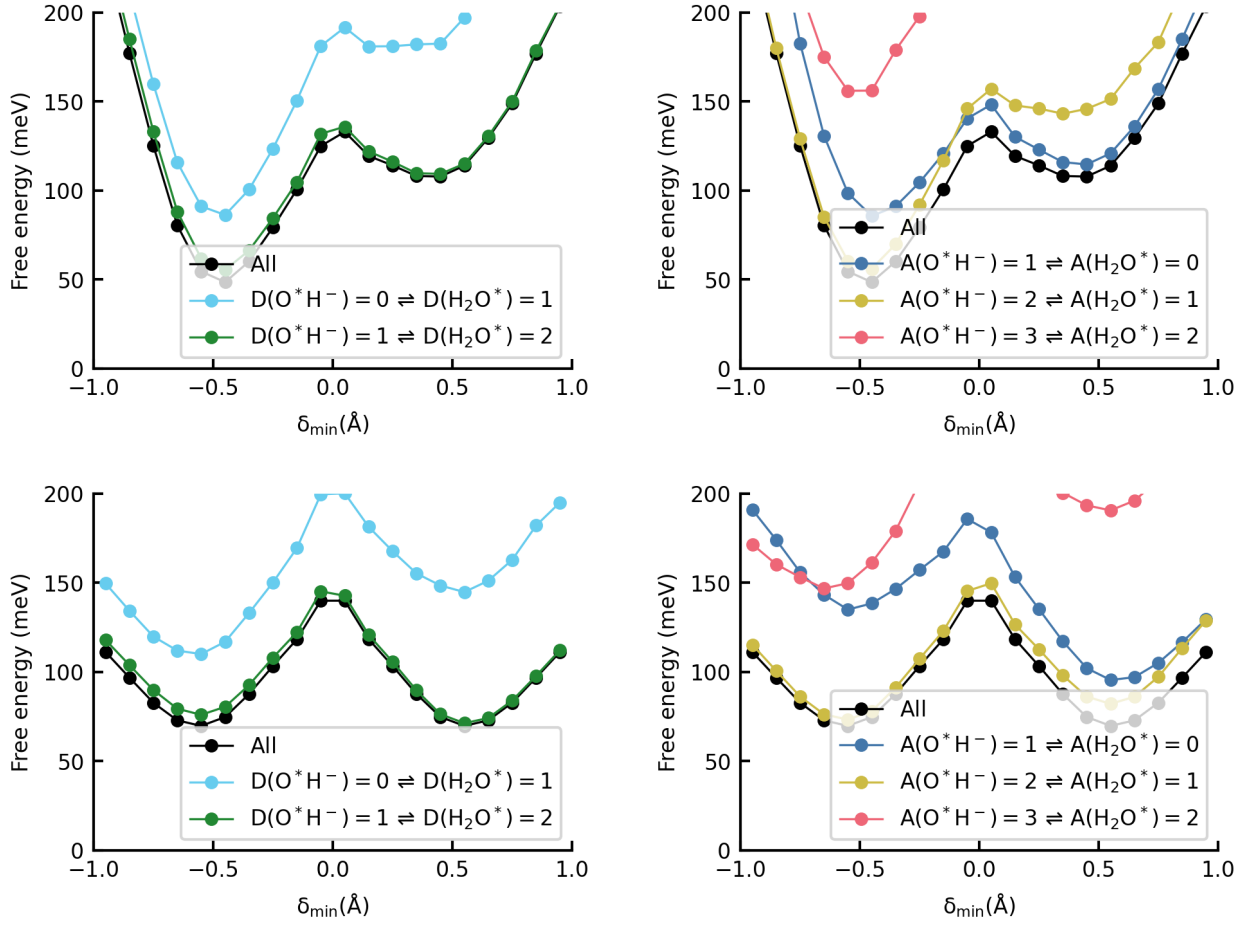


Figure 15: Free energy for  $CV = \delta_{\min}$  of surface-PT (top) and adlayer-PT (bottom) for the number of hydrogen bonds, where  $O^*H^-$  in left-hand side ( $H_2O^*$  in right-hand side) is the donor (D) or acceptor (A) in  $ZrO_2$ . The PT reaction formulas are summarised in the Table 1.

Figure 15 has been drawn in the same way as the Figure 14 for  $\text{ZrO}_2$ . Similar to  $\text{Zr}_7\text{O}_8\text{N}_4$ , there is an crossing at the surface-PT and no crossing at the adlayer-PT. However, the difference is that the crossing is on the left-hand side instead of right-hand side. It is unclear why such changes occur depending on the presence or absence of defects.

Table 7: Percentage (top) and average (bottom) of the number of hydrogen bonds, where  $\text{O}^*\text{H}^-$  in left-hand side ( $\text{H}_2\text{O}^*$  in right-hand side) in PT formula is the donor (D) or acceptor (A) in  $\text{Zr}_7\text{O}_8\text{N}_4$  and  $\text{ZrO}_2$ . See also Figures 14 and 15. The PT reaction formulas are summarised in the Table 1.

percentage	$\text{Zr}_7\text{O}_8\text{N}_4$		$\text{ZrO}_2$	
	surface	adlayer	surface	adlayer
D( $\text{O}^*\text{H}^-$ )=0	28	23	27	10
1	72	77	73	90
A( $\text{O}^*\text{H}^-$ )=1	16	38	33	44
2	81	61	66	55
3	3	1	1	1
D( $\text{H}_2\text{O}^*$ )=1	12	23	9	10
2	88	77	91	90
A( $\text{H}_2\text{O}^*$ )=0	66	38	75	44
1	33	61	24	55
2	1	1	1	1
average	$\text{Zr}_7\text{O}_8\text{N}_4$		$\text{ZrO}_2$	
	surface	adlayer	surface	adlayer
D( $\text{O}^*\text{H}^-$ )	0.72	0.77	0.73	0.90
A( $\text{O}^*\text{H}^-$ )	1.87	1.63	1.68	1.57
D( $\text{H}_2\text{O}^*$ )	1.88	1.77	1.91	1.90
A( $\text{H}_2\text{O}^*$ )	0.35	0.63	0.24	0.57

Table 7 shows percentage and average of the number of hydrogen bonds, where  $\text{O}^*\text{H}^-$  in left-hand side ( $\text{H}_2\text{O}^*$  in right-hand side) in PT formula is the donor (D) or acceptor (A). In the case of ZnO in previous research,<sup>23</sup> the more (less)  $\text{O}^*\text{H}^-$  ( $\text{H}_2\text{O}^*$ ) gives and accepts fewer (more) hydrogen bonds, the smaller the free energy barrier becomes. Furthermore, the average size of the hydrogen bonds given (accepted) explains why the barrier is smaller in the adlayer-PT than in the surface-PT. In the case of  $\text{Zr}_7\text{O}_8\text{N}_4$  and  $\text{ZrO}_2$  in this study, the average size relationship of the number of hydrogen bonds is the same as that of ZnO, but the shape of the free energy is different, so a similar argument does not hold.

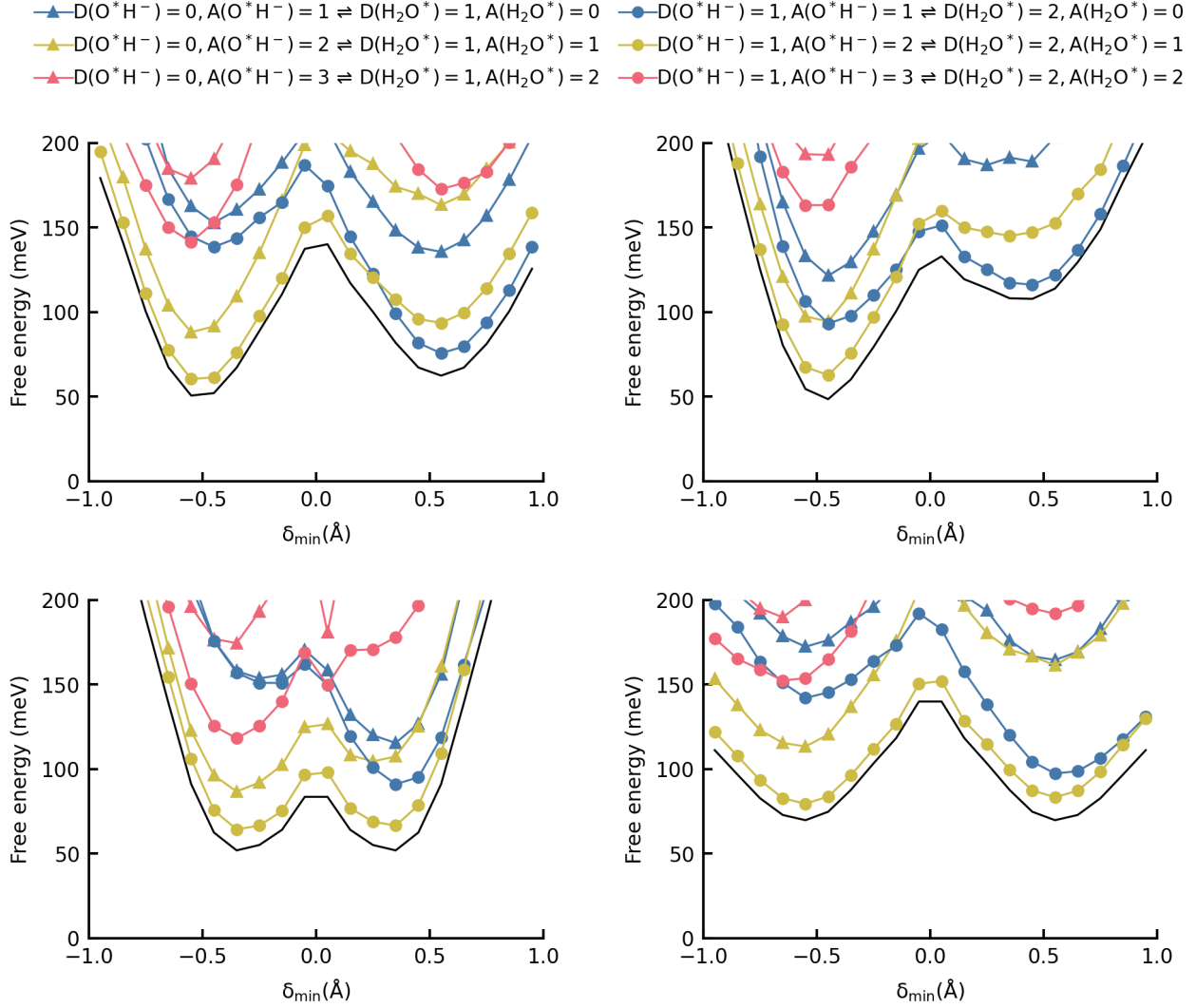


Figure 16: Free energy of surface-PT (top) and adlayer-PT (bottom) for the number of hydrogen bonds, where  $O^*H^-$  in left-hand side ( $H_2O^*$  in right-hand side) is the donor (D) and acceptor (A) in  $Zr_7O_8N_4$  (left),  $ZrO_2$  (right). In Figure 14 and Figure 15, the classification is based on D or A only. Here, the classification is based on the combination of D and A. The PT reaction formulas are summarised in the Table 1.



Figure 16 shows free energy of surface-PT and adlayer-PT for the number of hydrogen bonds, where  $\text{O}^*\text{H}^-$  in left-hand side ( $\text{H}_2\text{O}^*$  in right-hand side) is the donor and acceptor. In Figure 14 and Figure 15, the classification is based on D or A only. In this Figure, the classification is based on the combination of D and A. The PT reaction formulas are summarised in the Table 1. From Figure 14 and Figure 15, it was said that they cross at  $A(\text{H}_2\text{O}^*)=0$  and 1. From this figure we can see in more detail that  $D(\text{H}_2\text{O}^*),A(\text{H}_2\text{O}^*) = 2,0$  and  $2,1$  cross.

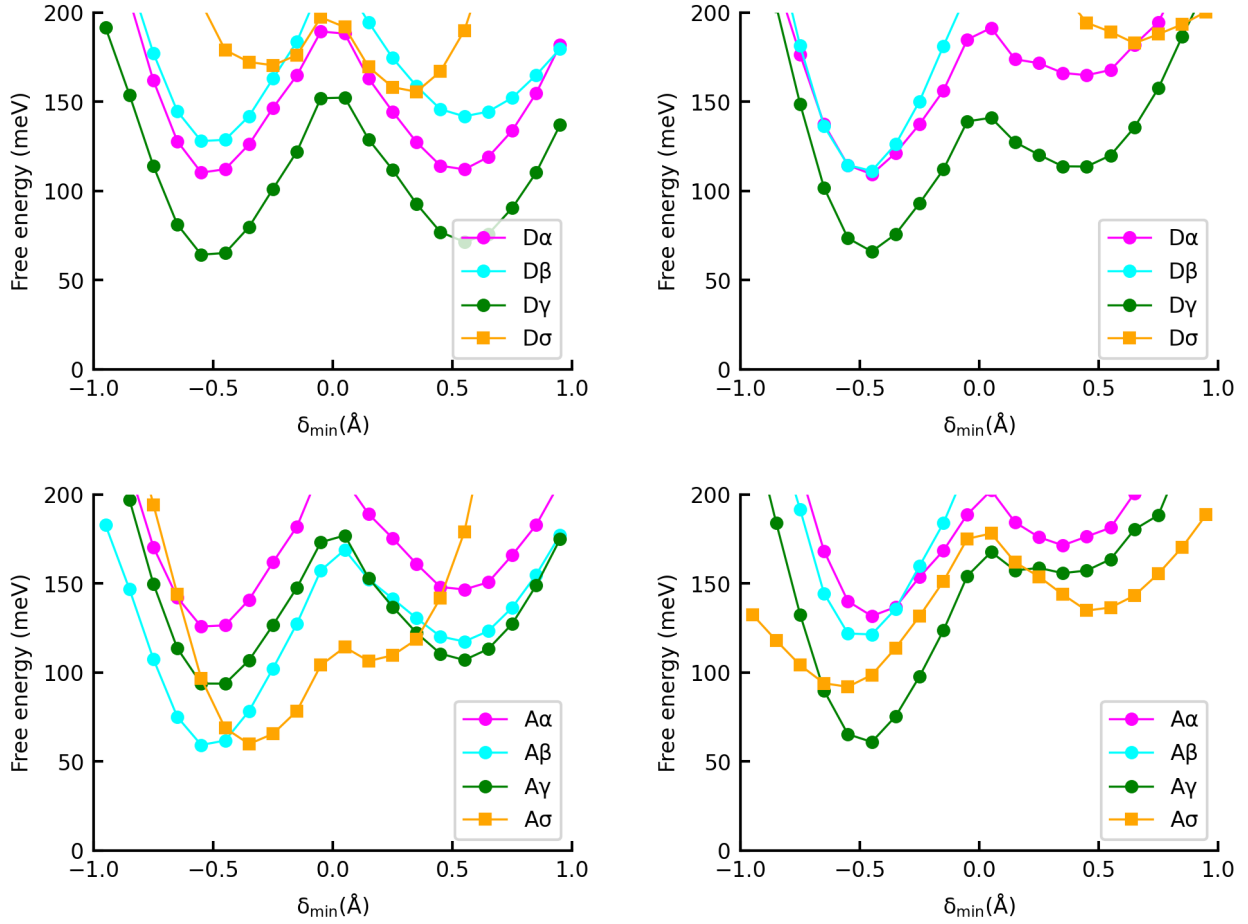


Figure 17: Free energy for  $\text{CV} = \delta_{\min}$  of surface-PT or adlayer-PT for the partner of hydrogen bonds, where  $\text{O}^*\text{H}^-$  in left-hand side ( $\text{H}_2\text{O}^*$  in right-hand side) is the donor (top) or acceptor (bottom) in  $\text{Zr}_7\text{O}_8\text{N}_4$  (left),  $\text{ZrO}_2$  (right).  $\text{D}\alpha, \text{D}\beta, \text{D}\gamma$  mean  $\text{O}^*\text{H}^-$  in surface-PT is a hydrogen bond donor with  $\text{O}^*\text{H}^-$ ,  $\text{H}_2\text{O}^*$ ,  $\text{H}_2\text{O}^\sim$ , respectively.  $\text{D}\sigma$  means  $\text{O}^*\text{H}^-$  in adlayer-PT is a hydrogen bond donor with  $\text{O}_s^{2-}$ .  $\text{A}\alpha, \beta, \gamma, \sigma$  are similar symbols for acceptors. Free energy properties (minimum, maximum and barriers) are shown in Table 8. The PT reaction formulas are summarised in the Table 1.

Figure 17 represents free energy for  $\text{CV} = \delta_{\min}$  of surface-PT or adlayer-PT for the partner of hydrogen bonds, where  $\text{O}^*\text{H}^-$  in left-hand side ( $\text{H}_2\text{O}^*$  in right-hand side) is the donor or acceptor.  $\text{D}\alpha, \beta, \gamma$  mean  $\text{O}^*\text{H}^-$  in surface-PT is a hydrogen bond donor with  $\text{O}^*\text{H}^-$ ,  $\text{H}_2\text{O}^*$ ,  $\text{H}_2\text{O}^\sim$ , respectively.  $\text{D}\sigma$  means  $\text{O}^*\text{H}^-$  in adlayer-PT is a hydrogen bond donor with  $\text{O}_s^{2-}$ .  $\text{A}\alpha, \text{A}\beta, \text{A}\gamma, \text{A}\sigma$  are similar symbols for acceptors. Free energy properties (minimum, maximum and barriers) are shown in Table 8. The PT reaction formulas are summarised in the Table 1. In previous research on  $\text{ZnO}$ ,<sup>23</sup> the minimum values of the free energy in

the right-hand side of  $D\alpha$  and  $D\sigma$  and in the left-hand side of  $A\beta$  and  $A\sigma$  are close to each other. This suggests that these states are competitive. In this study, the minimum values of  $A\beta$  and  $A\sigma$  are close, but the minimum values of  $D\alpha$  and  $D\sigma$  are far apart.

Table 8: Free energy properties (meV) for  $CV = \delta_{\min}$  of surface-PT and adlayer-PT for the partner of hydrogen bonds, where  $O^*H^-$  in left-hand side ( $H_2O^*$  in right-hand side) is the donor (top) or acceptor (bottom) in  $Zr_7O_8N_4$  and  $ZrO_2$  (See also Figure 17). LHS, RHS: left- and right-hand sides minimum. MAX: maximum. FW, BW: forward ( $\rightarrow$ ) and backward ( $\leftarrow$ ) PT barriers. The PT reaction formulas are summarised in the Table 1.

$Zr_7O_8N_4$	LHS	FW	MAX	BW	RHS
surface-PT $D\alpha$	110	79	189	77	112
surface-PT $D\beta$	128	88	216	74	142
surface-PT $D\gamma$	64	88	152	81	71
adlayer-PT $D\sigma$	170	27	197	41	156
surface-PT $A\alpha$	126	88	214	67	147
surface-PT $A\beta$	59	110	169	52	117
surface-PT $A\gamma$	94	87	177	70	107
adlayer-PT $A\sigma$	60	54	114	8	106
$ZrO_2$	LHS	FW	MAX	BW	RHS
surface-PT $D\alpha$	109	82	191	26	165
surface-PT $D\beta$	111	118	229	21	208
surface-PT $D\gamma$	66	75	141	27	114
adlayer-PT $D\sigma$	205	93	298	115	183
surface-PT $A\alpha$	132	70	202	31	171
surface-PT $A\beta$	121	112	233	15	218
surface-PT $A\gamma$	61	107	168	12	156
adlayer-PT $A\sigma$	92	86	178	43	135

In surface PT, the least common hydrogen bond partner (high free energy) is often  $H_2O^*$  ( $\beta$ ). However, as an exception,  $A\alpha$  has a higher free energy than  $A\beta$  in  $Zr_7O_8N_4$ . Following previous research on  $ZnO$ ,<sup>23</sup> we compare the maximum free energy values, assuming that the relative velocity between two PT mechanisms i and j (including both forward and backward reactions) is  $r_i/r_j = \exp(-MAX_i/k_B T)/\exp(-MAX_j/k_B T)$ . In  $Zr_7O_8N_4$ , the relative velocities are close in  $D\alpha$  and  $D\sigma$ ,  $A\beta$  and  $A\gamma$ , and in  $ZrO_2$ ,  $A\gamma$  and  $A\sigma$ . The adlayer PT ( $A\sigma$ ) has a lower barrier in competitive PT ( $A\beta$  and  $A\sigma$ ), but the adlayer PT ( $D\sigma$ ) has a higher barrier in non-competitive PT ( $D\alpha$  and  $A\sigma$ ). From the perspective of  $H_2O^*$ , which provides protons,  $D\alpha$  is lower in left-hand side, and  $D\sigma$  is lower in right-hand side. In  $ZrO_2$ ,

the free energies of  $D\alpha$  and  $D\beta$  are almost the same at left-hand side, but  $\alpha$  is significantly more stable than  $\beta$  at right-hand side, indicating that it is more preferred as an acceptor for hydrogen bond.

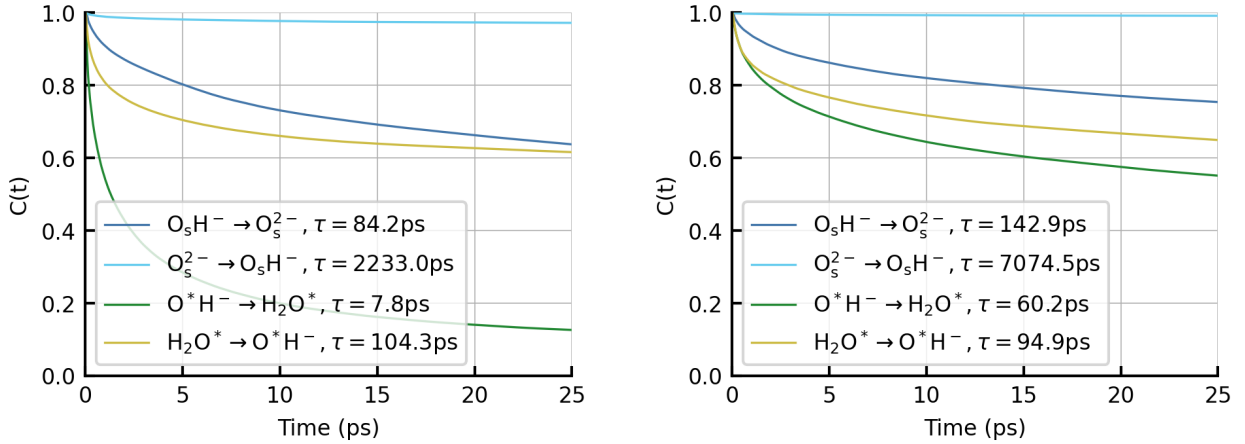


Figure 18: Time dependence of correlation function  $C(t)$  of surface-PT and adlayer-PT in  $Zr_7O_8N_4$  (left),  $ZrO_2$  (right). The PT reaction formulas are summarised in the Table 1.

Figure 18 shows time dependence of correlation function of surface-PT and adlayer-PT.  $Zr_7O_8N_4$  has a lower lifetime than  $ZrO_2$  for most PTs, which means faster proton transfer. The lifetime ratios,  $\tau(O_s^{2-} \rightarrow O_sH^-)/\tau(O_sH^- \rightarrow O_s^{2-})$ , are 26.5 and 49.5 for  $Zr_7O_8N_4$  and  $ZrO_2$  respectively. If this ratio is considered as the ease of dissociation,  $ZrO_2$  is easier to dissociate, which is consistent with the fact that defects reduce dissociative adsorption (Table 4).

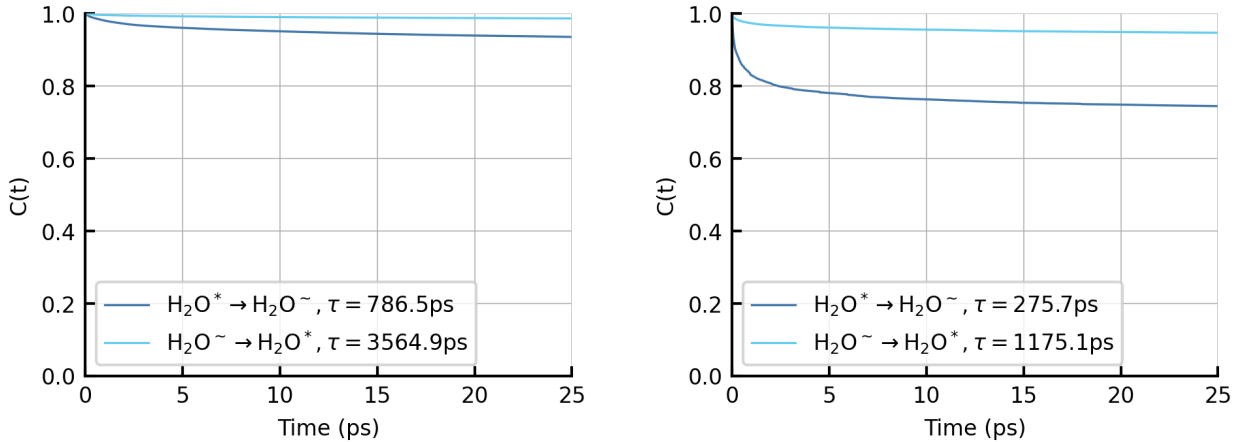


Figure 19: Time dependence of correlation function  $C(t)$  of water adsorption/desorption in  $Zr_7O_8N_4$  (left),  $ZrO_2$  (right).

Figure 19 shows time dependence of correlation function of water adsorption/desorption.

ZrO<sub>2</sub> has a shorter lifetime and water is easily released. In previous research,<sup>25</sup> based on their calculation results, ZnO(11 $\bar{2}$ 0) is easier to desorb adsorbed water than ZnO(10 $\bar{1}$ 0) (shorter lifetime), so the H<sub>2</sub>O\* → O\*H<sup>-</sup> reaction is less likely to occur (longer lifetime). In the case of this study, analogy does not hold because ZrO<sub>2</sub> has a shorter lifetime than Zr<sub>7</sub>O<sub>8</sub>N<sub>4</sub> for both reaction.

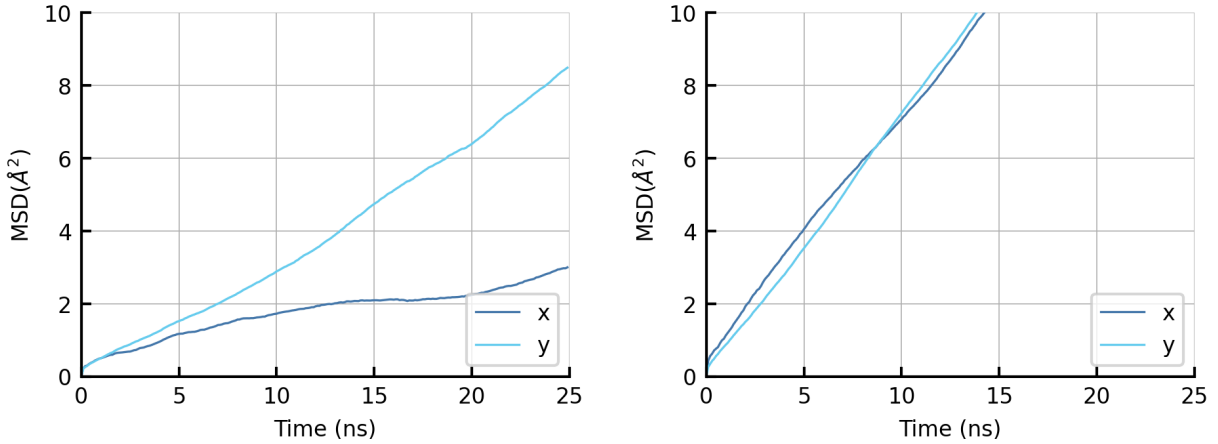


Figure 20: Mean squared displacement (MSD) of proton hole centers (PHCs) in  $\text{Zr}_7\text{O}_8\text{N}_4$  (left),  $\text{ZrO}_2$  (right).

Figure 20 shows mean squared displacement (MSD) of proton hole centers (PHCs). The diffusion coefficients ( $10^{-12} \text{ m}^2/\text{s}$ ) in the x and y directions calculated from this MSD are respectively  $\text{Zr}_7\text{O}_8\text{N}_4$  is (0.5, 1.7) and  $\text{ZrO}_2$  is (3.0, 3.7). While  $\text{ZrO}_2$  diffuses isotropically,  $\text{Zr}_7\text{O}_8\text{N}_4$  diffuses anisotropically and is small. Because  $\text{Zr}_7\text{O}_8\text{N}_4$  has defects, the adsorbate tends to concentrate (Figure 4). This is probably because adsorbates tend to be densely packed in  $\text{Zr}_7\text{O}_8\text{N}_4$  and even if an adlayer-PT often occurs between them, protons will circulate in the same place and will not contribute to effective diffusion.

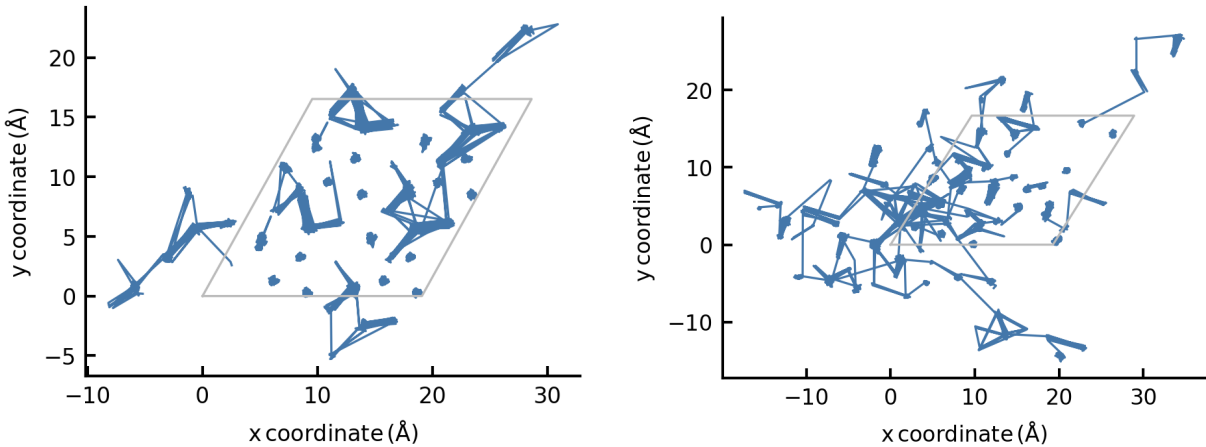


Figure 21: Trajectories of proton hole centers (PHCs) in  $\text{Zr}_7\text{O}_8\text{N}_4$  (left),  $\text{ZrO}_2$  (right).

Figure 21 shows trajectories of proton hole centers (PHCs). It can be seen that  $\text{ZrO}_2$  moves more from its initial position than  $\text{Zr}_7\text{O}_8\text{N}_4$ .

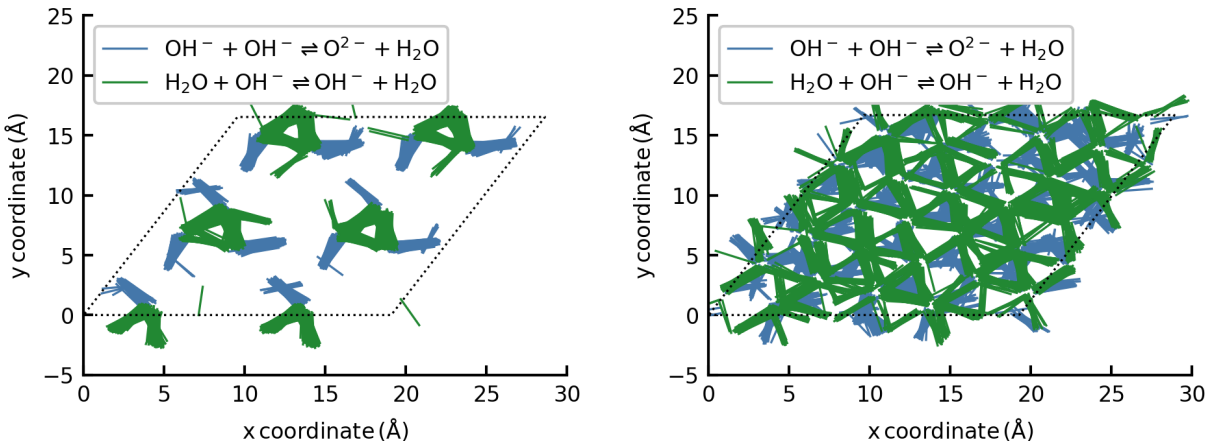


Figure 22: Pathways of PT in  $\text{Zr}_7\text{O}_8\text{N}_4$  (left),  $\text{ZrO}_2$  (right).

Figure 22 shows pathways of PT. It is thought that protons can only diffuse effectively over long distances through these PTs, depending on whether the paths in multiple PTs connect from a particular location within one cell to an equivalent location in a neighbouring cell. In  $\text{Zr}_7\text{O}_8\text{N}_4$ , PT pathways are clustered around  $V_{\text{O}}$  and do not connect from a location within a cell to an equivalent location in an adjacent cell. In  $\text{ZrO}_2$ , on the other hand, PT pathways exist throughout the cell, suggesting that they can connect from one cell to another. However, Figure 22 was calculated from 100 trajectories of 50 ps MD, and it does not mean that protons move between different cells within 50 ps in a single trajectory. A longer-term MD is required for a more detailed discussion. In the case of the 50 ns MD trajectory mentioned above, the total duration is sufficient. However, due to file capacity constraints, the trajectories were recorded at 100 ps intervals, so PT judgments tend to be incorrect. Future tasks will include performing long-term MD at smaller time intervals to accurately examine PT trajectories and determine which PTs contribute to long-range diffusion.



## Anharmonic OH vibrational spectrum

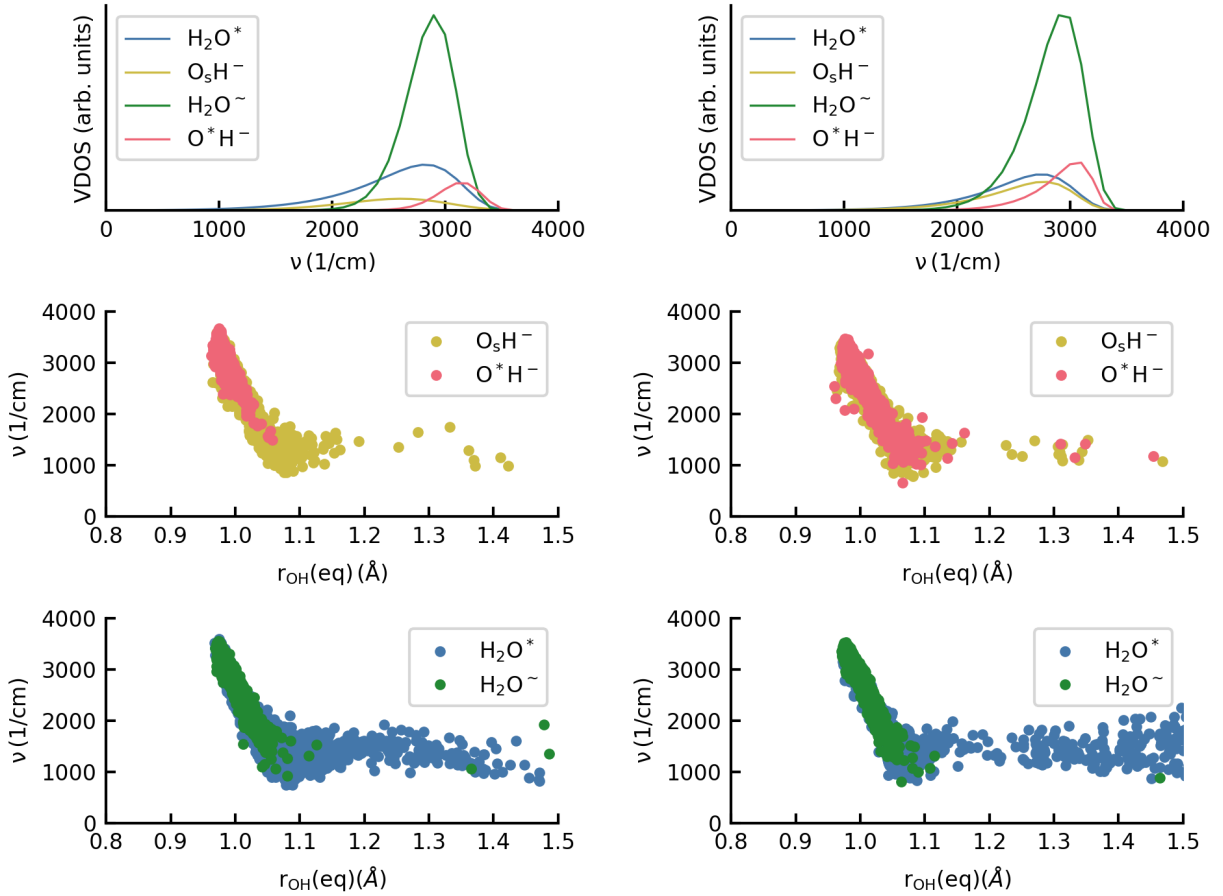


Figure 23: Vibrational density of states (VDOS) (top) and scatter plot of  $r_{\text{OH}}(\text{eq})$  and  $\nu_{\max}$  for OH (middle) and  $\text{H}_2\text{O}$  (bottom) in  $\text{Zr}_7\text{O}_8\text{N}_4$  (left),  $\text{ZrO}_2$  (right). Adsorbed oxygen, oxygen of the slab surface and oxygen in the solvent are expressed as  $\text{O}^*$ ,  $\text{O}_s$  and  $\text{O}^-$  respectively.

The upper part of Figure 23 shows the OH vibrational density of states (VDOS) for each oxygen state. Adsorbed oxygen, oxygen of the slab surface and oxygen in the solvent are expressed as  $\text{O}^*$ ,  $\text{O}_s$  and  $\text{O}^-$  respectively. For  $\text{O}_s\text{H}^-$ , the frequency  $\nu_{\max}$  was lowered (red shift) due to the defect. As mentioned above, the presence of the defect reduces the dissociative adsorption, so the surface PT reaction  $\text{O}_s\text{H}^- \rightarrow \text{O}_s^{2-}$  is more likely to occur than the reverse reaction, which is likely due to the broadening of the bottom of the potential  $V(r_{\text{OH}})$ . Conversely, for  $\text{O}^*\text{H}^-$  the frequency  $\nu_{\max}$  increases due to defects (blue shift). The reason for this is still not well understood. The middle and lower parts of Figure 23 are

scatter plots of the frequency  $\nu$  and the equilibrium distance  $r_{\text{OH}}(\text{eq})$  for each oxygen state. There is a negative correlation between  $\nu$  and  $r_{\text{OH}}(\text{eq})$ . This is because the weaker the OH bond, the lower the  $\nu$  and the longer  $r_{\text{OH}}(\text{eq})$ .

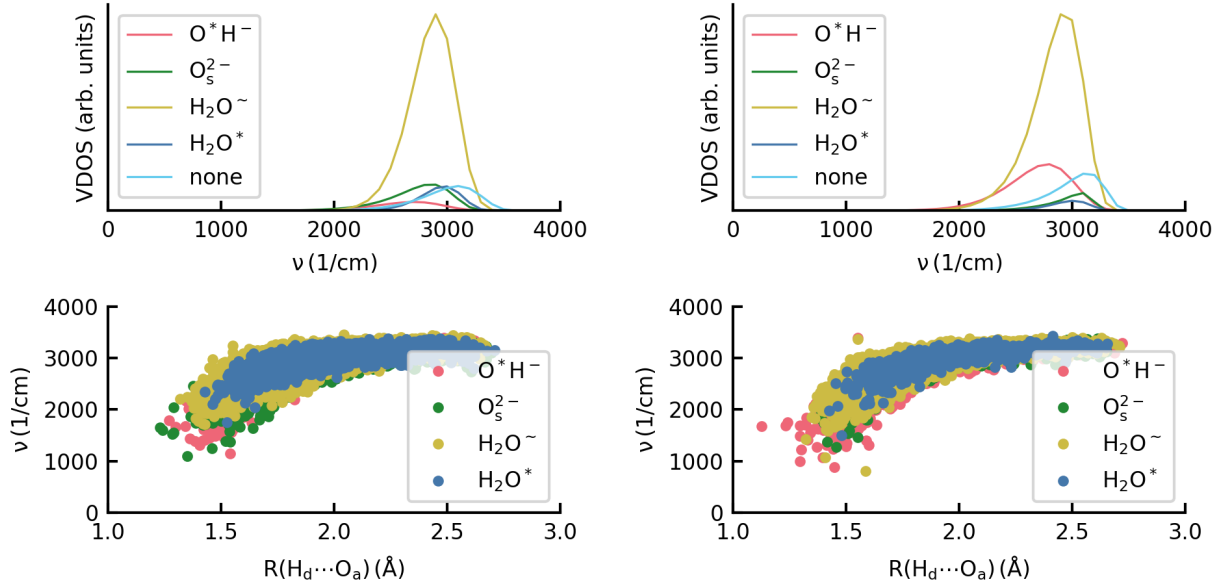


Figure 24: VDOS of  $\text{H}_2\text{O}^{\sim}$  for each acceptor of  $\text{Zr}_7\text{O}_8\text{N}_4$  (left),  $\text{ZrO}_2$  (right).

The upper part of Figure 24 represents the VDOS when O in  $\text{H}_2\text{O}^{\sim}$  is the hydrogen bond donor and the acceptors are  $\text{O}^*\text{H}^-$ ,  $\text{O}_s^{2-}$ ,  $\text{H}_2\text{O}^{\sim}$ ,  $\text{H}_2\text{O}^*$ , and none. The lower part of Figure 24 is a scatter plot of  $\nu$  and the distance  $R(\text{H}_d \cdots \text{O}_a)$  between the acceptors O and donated H. In  $\text{Zr}_7\text{O}_8\text{N}_4$ ,  $\nu_{\text{max}}$  decreases when the acceptor is  $\text{O}_s^{2-}$ , but the reason is unknown. For other acceptors,  $\nu_{\text{max}}$  is almost the same depending on whether there is a defect or not.

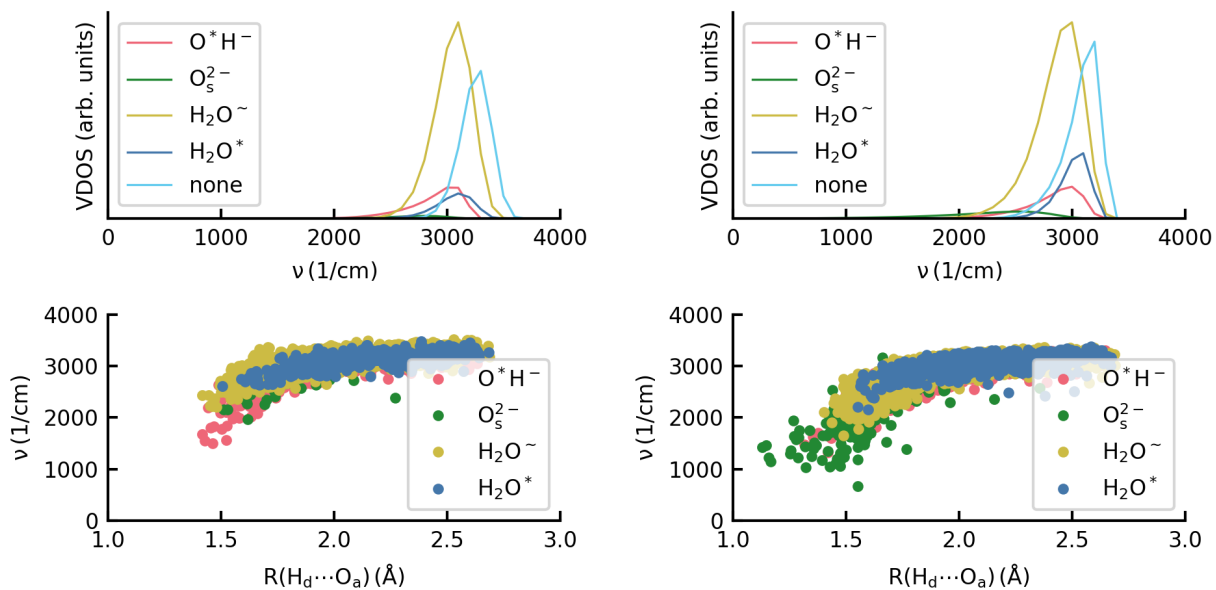


Figure 25: VDOS of  $\text{O}^*\text{H}^-$  for each acceptor of  $\text{Zr}_7\text{O}_8\text{N}_4$  (left),  $\text{ZrO}_2$  (right).

Figure 25 has been drawn in the same way as the Figure 24 for the case where O in  $\text{O}^*\text{H}^-$  is the hydrogen bond donor and the acceptors are  $\text{O}^*\text{H}^-$ ,  $\text{O}_s^{2-}$ ,  $\text{H}_2\text{O}^\sim$ ,  $\text{H}_2\text{O}^*$ , and none. In the scatter plot below, the samples are distributed in an elongated shape. This is because the hydrogen bonding environment has a uniform effect on the correlation between hydrogen bonds and vibrational frequency.

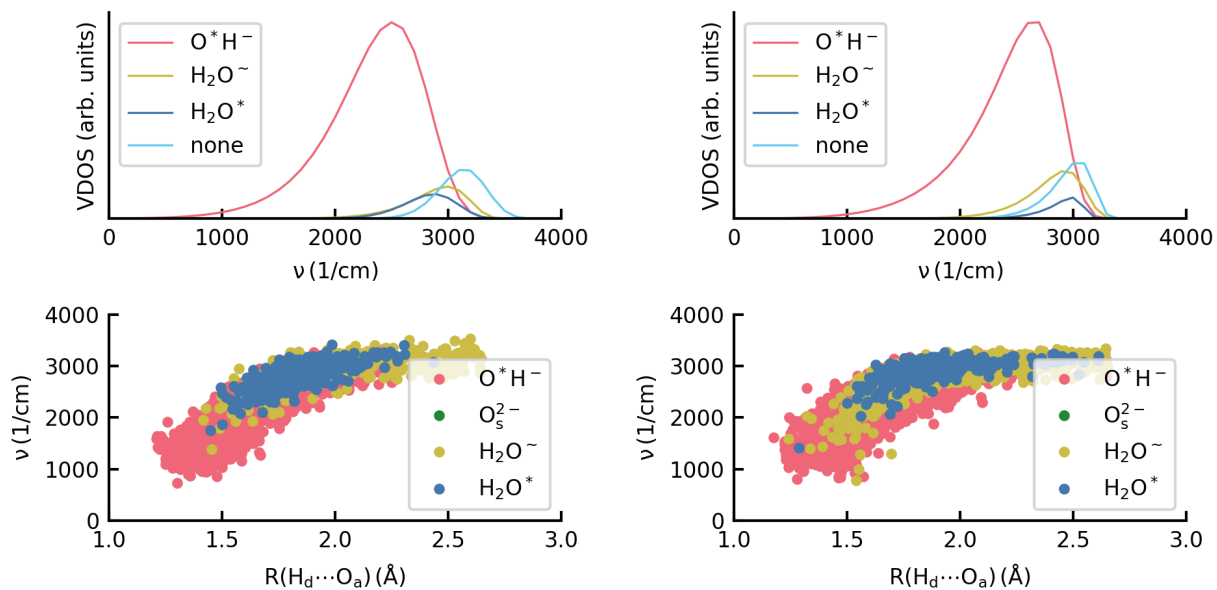


Figure 26: VDOS of  $\text{O}_s^{2-}$  for each acceptor of  $\text{Zr}_7\text{O}_8\text{N}_4$  (left),  $\text{ZrO}_2$  (right).

Figure 26 has been drawn in the same way as the Figure 24 for the case where O in  $\text{O}_s\text{H}^-$  is the hydrogen bond donor and the acceptors are  $\text{O}^*\text{H}^-$ ,  $\text{H}_2\text{O}^\sim$ ,  $\text{H}_2\text{O}^*$ , and none. The data for the acceptor  $\text{O}_s^{2-}$  are too small (less than 10) and are therefore omitted. As  $\text{O}^*\text{H}^-$  is involved in the surface PT, its  $\nu_{\text{max}}$  as an acceptor is the lowest.

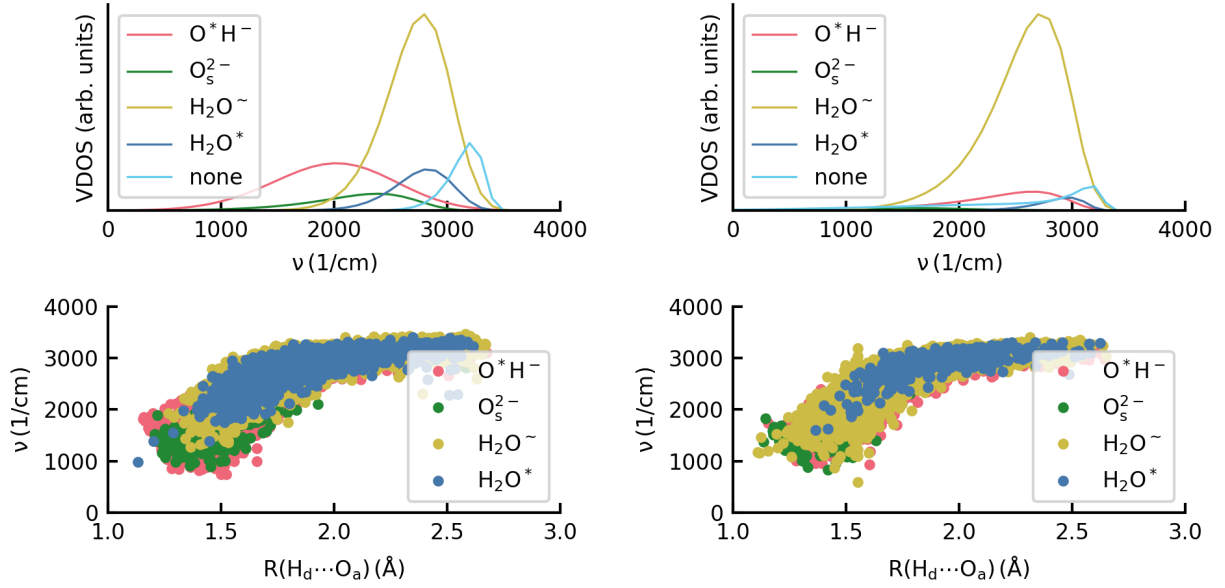


Figure 27: VDOS of  $\text{H}_2\text{O}^*$  for each acceptor of  $\text{Zr}_7\text{O}_8\text{N}_4$  (left),  $\text{ZrO}_2$  (right).

Figure 27 has been drawn in the same way as the Figure 24 for the case where O in  $\text{H}_2\text{O}^*$  is the hydrogen bond donor and the acceptors are  $\text{O}^*\text{H}^-$ ,  $\text{O}_s^{2-}$ ,  $\text{H}_2\text{O}^{\sim}$ ,  $\text{H}_2\text{O}^*$ , and none.  $\nu_{\max}$  is low when the acceptor is  $\text{O}^*\text{H}^-$  or  $\text{O}_s^{2-}$ . This is because each is related to the adlayer PT and the surface PT. Since  $\text{ZrO}_2$  is easily dissociated, the  $\nu_{\max}$  of  $\text{O}_s^{2-}$  is lower than that of  $\text{Zr}_7\text{O}_8\text{N}_4$ .

Table 9:  $\nu_{\max}$  at which the VDOS is maximum, the distance  $R_{\max}$  at which the histogram of the distance  $R(H_d \cdots O_a)$  is maximum and the number of data  $N_{\text{data}}$  for each hydrogen bond donor (D) and acceptor (A).

		Zr <sub>7</sub> O <sub>8</sub> N <sub>4</sub>					ZrO <sub>2</sub>
D	A	$\nu_{\max}$	$R_{\max}$	$N_{\text{data}}$	$\nu_{\max}$	$R_{\max}$	$N_{\text{data}}$
H <sub>2</sub> O <sup>~</sup>	O*H <sup>-</sup>	2675	1.625	1898	2747	1.675	7856
	O <sub>s</sub> <sup>2-</sup>	2814	1.775	4764	3041	1.825	1774
	H <sub>2</sub> O <sup>~</sup>	2886	1.775	27949	2910	1.775	25022
	H <sub>2</sub> O*	2956	1.825	3136	2991	1.825	1066
	none	3061		4280	3091		4932
	total	2889		42027	2910		40650
O*H <sup>-</sup>	O*H <sup>-</sup>	2995	2.075	537	2929	1.925	722
	O <sub>s</sub> <sup>2-</sup>	2756	1.625	63	2420	1.675	334
	H <sub>2</sub> O <sup>~</sup>	3076	1.875	2715	2935	1.825	4095
	H <sub>2</sub> O*	3095	2.125	349	3049	2.025	932
	none	3266		1681	3142		2964
	total	3132		5345	3015		9047
O <sub>s</sub> H <sup>-</sup>	O*H <sup>-</sup>	2451	1.675	4062	2579	1.625	6639
	O <sub>s</sub> <sup>2-</sup>			0			5
	H <sub>2</sub> O <sup>~</sup>	2949	1.825	435	2892	1.825	1083
	H <sub>2</sub> O*	2854	1.875	307	2956	1.875	314
	none	3135		541	3020		1006
	total	2570		5345	2692		9047
H <sub>2</sub> O*	O*H <sup>-</sup>	2008	1.525	4403	2543	1.675	1149
	O <sub>s</sub> <sup>2-</sup>	2313	1.675	1294	1615	1.475	187
	H <sub>2</sub> O <sup>~</sup>	2767	1.775	9666	2674	1.725	8823
	H <sub>2</sub> O*	2809	1.725	1879	2932	1.775	376
	none	3194		1761	2948		1204
	total	2743		19003	2675		11739

Table 9 shows the frequency  $\nu_{\max}$  at which the VDOS is maximum, the distance  $R_{\max}$  at which the histogram of the distance  $R(H_d \cdots O_a)$  is maximum and the number of data  $N_{\text{data}}$  for each hydrogen bond donor (D) and acceptor (A). There is nothing special to discuss on the basis of this table alone.

The Figure 28 summarises the frequency  $\nu_{\max}$  at which the VDOS becomes maximum. When the acceptor is H<sub>2</sub>O\*, most of the  $\nu_{\max}$  are higher than the total (except when the donor is O\*H<sup>-</sup> in Zr<sub>7</sub>O<sub>8</sub>N<sub>4</sub>). When the acceptor is O\*H<sup>-</sup>, all the  $\nu_{\max}$  are lower than the total. This is because O\*H<sup>-</sup> is a good acceptor, accepting H in both the surface PT and the

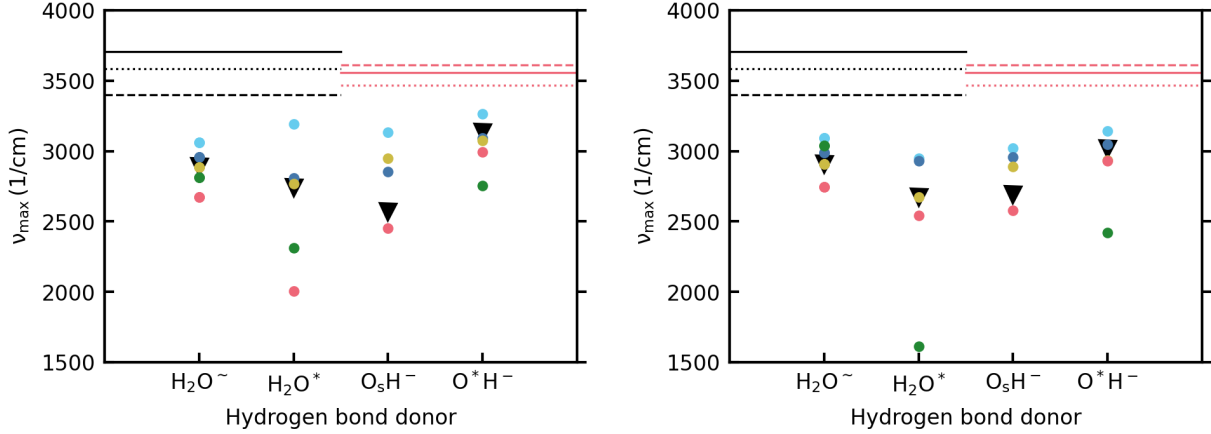
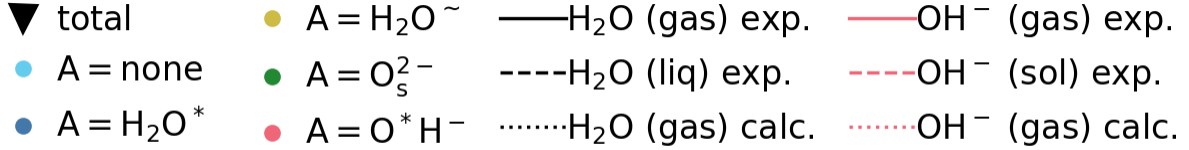


Figure 28: Summary of  $\nu_{\max}$  for H<sub>2</sub>O and OH of Zr<sub>7</sub>O<sub>8</sub>N<sub>4</sub> (left), ZrO<sub>2</sub> (right). For comparison, we also show first-principles calculation data of gas phase H<sub>2</sub>O and OH<sup>-</sup>,<sup>24</sup> and experimental data of gas phase H<sub>2</sub>O,<sup>61</sup> liquid phase H<sub>2</sub>O,<sup>62</sup> gas phase OH<sup>-</sup>,<sup>63</sup> and solvated OH<sup>-</sup>,<sup>64</sup>

adlayer PT. All  $\nu_{\max}$  in this study are lower than experimental results and first-principles calculations.

Figure 29 is a scatter plot of the frequency  $\nu_{\max}$  where VDOS is maximum and the  $R_{\max}$  where the histogram of distance  $R(\text{H}_d \cdots \text{O}_a)$  is maximum. In addition, the correlation for each donor has been approximated by a linear function. There's nothing special to say about this.

Table 10: The slope of the linear function for  $\nu_{\max}$ - $R_{\max}$ , the range of  $R_{\max}$  and the full width at half maximum  $\gamma_0$  of the VDOS for each donor.

D	Zr <sub>7</sub> O <sub>8</sub> N <sub>4</sub>				ZrO <sub>2</sub>		
	slope	range	$\gamma_0$	slope	range	$\gamma_0$	
H <sub>2</sub> O*	3313	0.25	982	4356	0.3	876	
O <sub>5</sub> H <sup>-</sup>	2316	0.2	1089	1524	0.25	857	
H <sub>2</sub> O <sup>~</sup>	1326	0.2	505	1793	0.15	548	
O*H <sup>-</sup>	565	0.5	446	1715	0.35	492	

Table 10 summarises the slope of the linear function in the Figure 29, the range of



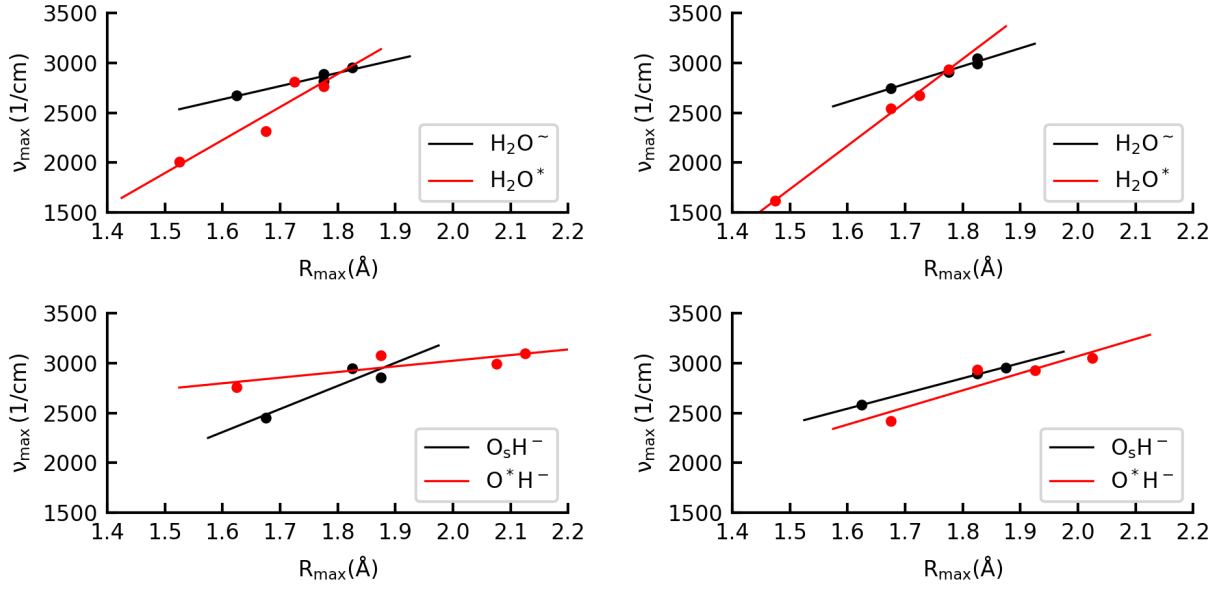


Figure 29:  $R_{\max}$  and  $\nu_{\max}$  of  $Zr_7O_8N_4$  (left),  $ZrO_2$  (right).

$R_{\max}$  (the difference between the maximum and minimum values) and the full width at half maximum  $\gamma_0$  of the VDOS for each donor. In ZnO, these orders coincide and are correlated.<sup>24</sup> In both  $Zr_7O_8N_4$  and  $ZrO_2$  the order does not match completely and there is no correlation as in previous studies.

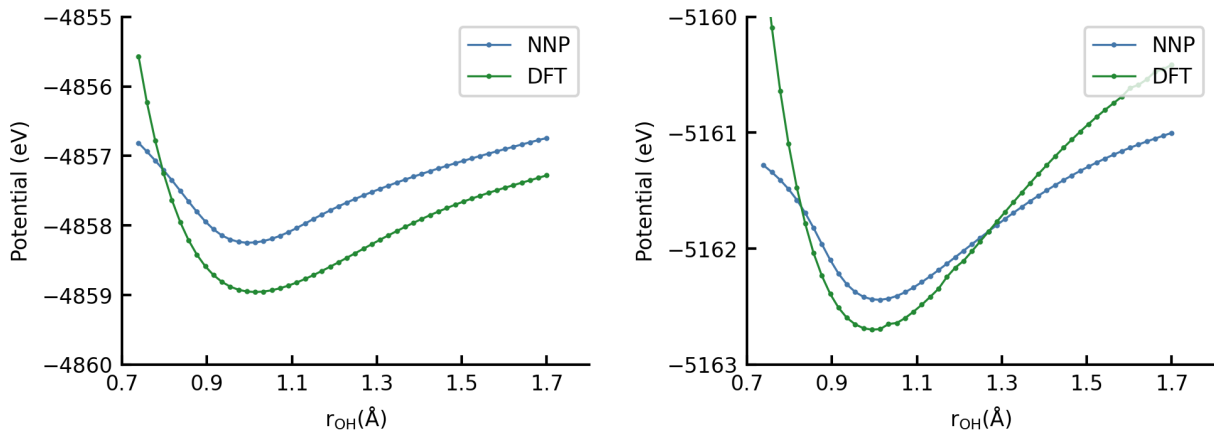


Figure 30: Potential energy for the OH bond distance  $r_{\text{OH}}$  of solvent water molecules calculated by NNP (blue) and DFT (green).

Figure 30 is an example of the potential energy for stretching and contracting the OH bond distance  $r_{\text{OH}}$  of solvent water molecules, calculated using NNP and Density Functional Theory (DFT). The RMSEs of energy in  $\text{Zr}_7\text{O}_8\text{N}_4, \text{ZrO}_2$  were 1.064, 0.661 (meV/atom). The frequencies of  $\text{Zr}_7\text{O}_8\text{N}_4$  calculated from the NNP and DFT potentials were 3084, 2969 (1/cm) and these of  $\text{ZrO}_2$  were 2853, 3302 (1/cm).  $\text{ZrO}_2$  has a smaller error in  $V(r_{\text{OH}})$ , but the difference in frequency is large, reaching more than 300 (1/cm). This is thought to be due to the change in curvature of the potential. This may be one of the causes of the problem mentioned above that the  $\nu_{\text{max}}$  calculated by NNP is far from the experimental values of the vibrational frequencies in  $\text{H}_2\text{O}$  and  $\text{OH}^-$ . A method to solve this problem has not yet been found. In addition, as for  $\text{ZrO}_2$ , if the potential in the range of  $r_{\text{OH}}(\text{eq}) \pm 0.2 \text{ \AA}$  is approximated by a quadratic polynomial (harmonic approximation), the calculated frequencies are 3079, 3081 (1/cm) (NNP, DFT). While the difference between NNP and DFT almost disappears, the difference to the 11th degree polynomial is large. This means that the influence of the anharmonic effect cannot be ignored.

## Future work

In addition to structural properties such as those in this study, other studies of solid/water interface systems using NNPMMD include that for water dissociation<sup>35,36</sup> and solvation dynamics.<sup>32</sup> Systems with intermediates in the ORR could also be added to the data to learn NNPs, sampled by NNPMMD and calculate the free energies on the reaction pathways, so that the influence of defects and the proportion of molecular and dissociative adsorption on catalytic activity could also be discussed. There is also much to be explored in studies based on conventional first-principles calculations. In contrast to the present study, there are previous studies that have discussed the electric double layer (EDL) by calculating the electrostatic potential and density when the system is about a system with ions in water.<sup>65–69</sup> For example, Ando et al. performed AIMD at the interface between Pt and water containing  $\text{Na}^+$  ions and calculated the electrostatic potential due to the EDL based on the difference in the potentials between the case with and without  $\text{Na}^+$  ions.<sup>65</sup> For  $\text{Zr}_7\text{O}_8\text{N}_4$  and  $\text{ZrO}_2$ , the electrostatic potential due to the EDL could also be evaluated in NNPMMD by training NNP with additional data for the case of the solvent containing ions. Alternatively, as in the work of Otani et al.,<sup>70</sup> the electrostatic potential of  $\text{H}_3\text{O}^+$  in oxygen can be discussed by creating a system with excess  $\text{H}^+$  and electrons in water and performing an AIMD based on the effective screening medium method. Other studies,<sup>71–74</sup> have performed AIMD and structural optimisation to discuss band offsets, which are important values in interface systems, taking into account electron affinity, charge neutrality level and pinning factor, and have discussed the band offset, which is an important value in interface systems. This multifaceted study will allow a more detailed investigation of the effects of defects at the oxide/water interface.

## Conclusion

In this study, NNPs were constructed by active learning for interfaces between the water and defective  $\text{Zr}_7\text{O}_8\text{N}_4$  or pristine  $\text{ZrO}_2$ . Based on 1000 NNPMMD trajectories, the structures

of water molecule adsorption on these interfaces were investigated and it was found that  $\text{Zr}_7\text{O}_8\text{N}_4$  has a bilayer structure, which is different from a monolayer structure of  $\text{ZrO}_2$ . On the  $\text{Zr}_7\text{O}_8\text{N}_4$  surface, water molecules do not adsorb on the  $\text{V}_\text{O}$  but only on some of the surrounding Zr atoms, suggesting that the  $\text{V}_\text{O}$  is expected to act as an active site for the ORR. While the proportion of dissociative adsorption in  $\text{Zr}_7\text{O}_8\text{N}_4$  is less than in  $\text{ZrO}_2$  due to the less oxygen on which the  $\text{H}^+$  can adsorb, the total number of molecular and dissociative adsorption is the same for both materials. Therefore,  $\text{Zr}_7\text{O}_8\text{N}_4$  may promote the ORR more than  $\text{ZrO}_2$  because the  $\text{V}_\text{O}$ s act as additional active sites. In the future, the influence of the solvent on the ORR activity of  $\text{Zr}_7\text{O}_8\text{N}_4$  could be discussed by updating the NNP with new data for systems with intermediate oxygen and hydrogen molecules in addition to the solvent, water molecules. We also calculated things that had been calculated in previous studies, such as the free energy of proton transfer and the vibrational density of states of OH. We hope that the various findings from this study will be useful for research into the solid-water interface.

## Acknowledgement

This research was supported by the New Energy and Industrial Technology Development Organization (NEDO) project, MEXT as “Program for Promoting Researches on the Supercomputer Fugaku” (Fugaku battery and Fuel Cell Project) (Grant No. JPMXP1020200301, Project No.: hp220177, hp210173, hp200131), and the Japan Society for the Promotion of Science (JSPS) as Grants in Aid for Scientific Research on Innovative Area “Hydrogenomics” (Grant No. 18H05519). The calculations were conducted at the ISSP Supercomputers Center, The University of Tokyo.

## References

- (1) Debe, M. K. Electrocatalyst approaches and challenges for automotive fuel cells. *Nature* **2012**, *486*, 43–51.
- (2) Doi, S.; Ishihara, A.; Mitsushima, S.; Kamiya, N.; Ota, K. Zirconium-Based Compounds for Cathode of Polymer Electrolyte Fuel Cell. *J. Electrochem. Soc.* **2007**, *154*, B362.
- (3) Chisaka, M.; Ishihara, A.; Morioka, H.; Nagai, T.; Yin, S.; Ohgi, Y.; Matsuzawa, K.; Mitsushima, S.; Ota, K. Zirconium Oxynitride-Catalyzed Oxygen Reduction Reaction at Polymer Electrolyte Fuel Cell Cathodes. *ACS Omega* **2017**, *2*, 678–684.
- (4) Ishihara, A. et al. Emergence of Oxygen Reduction Activity in Zirconium Oxide-Based Compounds in Acidic Media: Creation of Active Sites for the Oxygen Reduction Reaction. *J. Phys. Chem. C* **2019**, *123*, 18150–18159.
- (5) Arashi, T.; Seo, J.; Takanabe, K.; Kubota, J.; Domen, K. Nb-doped TiO<sub>2</sub> cathode catalysts for oxygen reduction reaction of polymer electrolyte fuel cells. *Catal. Today* **2014**, *233*, 181–186.
- (6) Ishihara, A.; Arao, M.; Matsumoto, M.; Tokai, T.; Nagai, T.; Kuroda, Y.; Matsuzawa, K.; Imai, H.; Mitsushima, S.; Ota, K. Niobium-added titanium oxides powders as non-noble metal cathodes for polymer electrolyte fuel cells – Electrochemical evaluation and effect of added amount of niobium. *Int. J. Hydrog. Energy* **2020**, *45*, 5438–5448.
- (7) Ishihara, A.; Hamazaki, M.; Arao, M.; Matsumoto, M.; Imai, H.; Kohno, Y.; Matsuzawa, K.; Mitsushima, S.; Ota, K. Titanium-Niobium Oxides Mixed with Ti<sub>4</sub>O<sub>7</sub> as Precious-Metal- and Carbon-Free Cathodes for Polymer Electrolyte Fuel Cells. *J. Electrochem. Soc.* **2016**, *163*, F603.

- (8) Ishihara, A.; Wu, C.; Nagai, T.; Ohara, K.; Nakada, K.; Matsuzawa, K.; Napporn, T.; Arao, M.; Kuroda, Y.; Tominaka, S.; Mitsushima, S.; Imai, H.; Ota, K. Factors affecting oxygen reduction activity of Nb<sub>2</sub>O<sub>5</sub>-doped TiO<sub>2</sub> using carbon nanotubes as support in acidic solution. *Electrochim. Acta* **2018**, *283*, 1779–1788.
- (9) Ishihara, A.; Tominaka, S.; Mitsushima, S.; Imai, H.; Sugino, O.; Ota, K. Challenge of advanced low temperature fuel cells based on high degree of freedom of group 4 and 5 metal oxides. *Curr. Opin. Electrochem.* **2020**, *21*, 234–241.
- (10) Ota, K.; Ohgi, Y.; Matsuzawa, K.; Mitsushima, S.; Ishihara, A. Transition Metal Oxide Based Materials for Cathode of Polymer Electrolyte Fuel Cells. *ECS Trans.* **2012**, *45*, 27.
- (11) Ukita, K.; Ishihara, A.; Ohgi, Y.; Matsuzawa, K.; Mitsushima, S.; Ota, K. Zirconium Oxide-Based Compounds as Non-Pt Cathode for Polymer Electrolyte Fuel Cell. *Electrochemistry* **2011**, *79*, 340–342.
- (12) Yin, S.; Ishihara, A.; Kohno, Y.; Matsuzawa, K.; Mitsushima, S.; Ota, K.; Matsumoto, M.; Imai, H. Enhancement of Oxygen Reduction Activity of Zirconium Oxide-Based Cathode for PEFC. *ECS Trans.* **2013**, *58*, 1489.
- (13) Bredow, T.; Lerch, M. Anion Distribution in Zr<sub>2</sub>ON<sub>2</sub>. *Z. Anorg. Allg. Chem.* **2004**, *630*, 2262–2266.
- (14) Bredow, T.; Lerch, M. On the Anion Distribution in Zr<sub>7</sub>O<sub>8</sub>N<sub>4</sub>. *Z. Anorg. Allg. Chem.* **2007**, *633*, 2598–2602.
- (15) Maekawa, Y.; Ishihara, A.; Kim, J.-H.; Mitsushima, S.; Ota, K.-i. Catalytic Activity of Zirconium Oxynitride Prepared by Reactive Sputtering for ORR in Sulfuric Acid. *Electrochem. Solid-State Lett.* **2008**, *11*, B109.

- (16) Yamamoto, Y.; Kasamatsu, S.; Sugino, O. Scaling Relation of Oxygen Reduction Reaction Intermediates at Defective TiO<sub>2</sub> Surfaces. *J. Phys. Chem. C* **2019**, *123*, 19486–19492.
- (17) Muhammady, S.; Haruyama, J.; Kasamatsu, S.; Sugino, O. Tuning Oxygen Reduction on Monoclinic and Tetragonal Zirconia Surfaces Using Oxygen Vacancy and Nitrogen Doping: A Density-Functional Study. *Meet. Abstr.* **2022**, *MA2022-01*, 1517.
- (18) Muhammady, S.; Haruyama, J.; Kasamatsu, S.; Sugino, O. Effect of Nitrogen Doping and Oxygen Vacancy on the Oxygen Reduction Reaction on the Tetragonal Zirconia (101) Surface. *J. Phys. Chem. C* **2022**, *126*, 15662–15670.
- (19) Nørskov, J. K.; Rossmeisl, J.; Logadottir, A.; Lindqvist, L.; Kitchin, J. R.; Bligaard, T.; Jónsson, H. Origin of the Overpotential for Oxygen Reduction at a Fuel-Cell Cathode. *J. Phys. Chem. B* **2004**, *108*, 17886–17892.
- (20) Behler, J.; Csányi, G. Machine learning potentials for extended systems: a perspective. *Eur. Phys. J. B* **2021**, *94*, 142.
- (21) Natarajan, S. K.; Behler, J. Neural network molecular dynamics simulations of solid–liquid interfaces: water at low-index copper surfaces. *Phys. Chem. Chem. Phys.* **2016**, *18*, 28704–28725.
- (22) Natarajan, S. K.; Behler, J. Self-Diffusion of Surface Defects at Copper–Water Interfaces. *J. Phys. Chem. C* **2017**, *121*, 4368–4383.
- (23) Quaranta, V.; Hellström, M.; Behler, J. Proton-Transfer Mechanisms at the Water–ZnO Interface: The Role of Presolvation. *J. Phys. Chem. Lett.* **2017**, *8*, 1476–1483.
- (24) Quaranta, V.; Hellström, M.; Behler, J.; Kullgren, J.; Mitev, P. D.; Hermansson, K. Maximally resolved anharmonic OH vibrational spectrum of the water/ZnO(10 $\bar{1}$ 0) in-

- terface from a high-dimensional neural network potential. *J. Chem. Phys.* **2018**, *148*, 241720.
- (25) Quaranta, V.; Behler, J.; Hellström, M. Structure and Dynamics of the Liquid–Water/Zinc-Oxide Interface from Machine Learning Potential Simulations. *J. Phys. Chem. C* **2019**, *123*, 1293–1304.
- (26) Artrith, N. Machine learning for the modeling of interfaces in energy storage and conversion materials. *J. Phys. Energy* **2019**, *1*, 032002.
- (27) Andrade, M. F. C.; Ko, H.; Zhang, L.; Car, R.; Selloni, A. Free energy of proton transfer at the water–TiO<sub>2</sub> interface from ab initio deep potential molecular dynamics. *Chem. Sci.* **2020**, *11*, 2335–2341.
- (28) Ghorbanfekr, H.; Behler, J.; Peeters, F. M. Insights into Water Permeation through hBN Nanocapillaries by Ab Initio Machine Learning Molecular Dynamics Simulations. *J. Phys. Chem. Lett.* **2020**, *11*, 7363–7370.
- (29) Eckhoff, M.; Behler, J. Insights into lithium manganese oxide–water interfaces using machine learning potentials. *J. Chem. Phys.* **2021**, *155*, 244703.
- (30) Schran, C.; Thiemann, F. L.; Rowe, P.; Müller, E. A.; Marsalek, O.; Michaelides, A. Machine learning potentials for complex aqueous systems made simple. *Proc. Natl. Acad. Sci. U.S.A.* **2021**, *118*, e2110077118.
- (31) Mikkelsen, A. E. G.; Schiøtz, J.; Vegge, T.; Jacobsen, K. W. Is the water/Pt(111) interface ordered at room temperature? *J. Chem. Phys.* **2021**, *155*, 224701.
- (32) Schienbein, P.; Blumberger, J. Nanosecond solvation dynamics of the hematite/liquid water interface at hybrid DFT accuracy using committee neural network potentials. *Phys. Chem. Chem. Phys.* **2022**, *24*, 15365–15375.



- (33) Mikkelsen, A. E. G.; Kristoffersen, H. H.; Schiøtz, J.; Vegge, T.; Hansen, H. A.; Jacobsen, K. W. Structure and energetics of liquid water–hydroxyl layers on Pt(111). *Phys. Chem. Chem. Phys.* **2022**, *24*, 9885–9890.
- (34) Fan, X.; Wen, X.; Zhuang, Y.; Cheng, J. Molecular insight into the GaP(110)–water interface using machine learning accelerated molecular dynamics. *J. Energy Chem.* **2023**,
- (35) Wen, B.; Andrade, M. F. C.; Liu, L.; Selloni, A. Water dissociation at the water–rutile TiO<sub>2</sub>(110) interface from ab initio-based deep neural network simulations. *Proc. Natl. Acad. Sci. U.S.A.* **2023**, *120*, e2212250120.
- (36) Zeng, Z.; Wodaczek, F.; Liu, K.; Stein, F.; Hutter, J.; Chen, J.; Cheng, B. Water dissociation on pristine low-index TiO<sub>2</sub> surfaces. *arXiv:2303.07433 [cond-mat.mtrl-sci]*
- (37) Artrith, N.; Urban, A.; Ceder, G. Efficient and accurate machine-learning interpolation of atomic energies in compositions with many species. *Phys. Rev. B* **2017**, *96*, 014112.
- (38) Kasamatsu, S.; Motoyama, Y.; Yoshimi, K.; Matsumoto, U.; Kuwabara, A.; Ogawa, T. Facilitating ab initio configurational sampling of multicomponent solids using an on-lattice neural network model and active learning. *J. Chem. Phys.* **2022**, *157*, 104114, Publisher: American Institute of Physics.
- (39) Hoshino, K.; Kasamatsu, S.; Hyodo, J.; Yamamoto, K.; Setoyama, H.; Okajima, T.; Yamazaki, Y. Probing Local Environments of Oxygen Vacancies Responsible for Hydration in Sc-Doped Barium Zirconates at Elevated Temperatures: In Situ X-ray Absorption Spectroscopy, Thermogravimetry, and Active Learning Ab Initio Replica Exchange Monte Carlo Simulations. *Chem. Mater.* **2023**, *35*, 2289–2301, Publisher: American Chemical Society.
- (40) Behler, J.; Parrinello, M. Generalized Neural-Network Representation of High-Dimensional Potential-Energy Surfaces. *Phys. Rev. Lett.* **2007**, *98*, 14601.

- (41) Behler, J. Constructing high-dimensional neural network potentials: A tutorial review. *Int. J. Quant. Chem.* **2015**, *115*, 1032–1050.
- (42) Momma, K.; Izumi, F. VESTA 3 for three-dimensional visualization of crystal, volumetric and morphology data. *J. Appl. Cryst.* **2011**, *44*, 1272–1276.
- (43) Kresse, G.; Furthmüller, J. Efficient iterative schemes for *ab initio* total-energy calculations using a plane-wave basis set. *Phys. Rev. B* **1996**, *54*, 11169.
- (44) <https://www.vasp.at/>.
- (45) Blöchl, P. E. Projector augmented-wave method. *Phys. Rev. B* **1994**, *50*, 17953.
- (46) Perdew, J. P.; Burke, K.; Ernzerhof, M. Generalized Gradient Approximation Made Simple. *Phys. Rev. Lett.* **1996**, *77*, 3865.
- (47) Lee, K.; Yoo, D.; Jeong, W.; Han, S. SIMPLE-NN: An efficient package for training and executing neural-network interatomic potentials. *Comput. Phys. Commun.* **2019**, *242*, 95–103.
- (48) <https://simple-nn-v2.readthedocs.io/en/latest/>.
- (49) Plimpton, S. Fast Parallel Algorithms for Short-Range Molecular Dynamics. *J. Comput. Phys.* **1995**, *117*, 1–19.
- (50) <https://www.lammps.org/>.
- (51) Tuckerman, M. E.; Marx, D.; Parrinello, M. The nature and transport mechanism of hydrated hydroxide ions in aqueous solution. *Nature* **2002**, *417*, 925–929.
- (52) Laage, D.; Hynes, J. T. On the Residence Time for Water in a Solute Hydration Shell: Application to Aqueous Halide Solutions. *J. Phys. Chem. B* **2008**, *112*, 7697–7701.

- (53) Hellström, M.; Quaranta, V.; Behler, J. One-dimensional vs. two-dimensional proton transport processes at solid–liquid zinc-oxide–water interfaces. *Chem. Sci.* **2019**, *10*, 1232–1243.
- (54) Mitev, P. D.; Eriksson, A.; Boily, J.-F.; Hermansson, K. Vibrational models for a crystal with 36 water molecules in the unit cell: IR spectra from experiment and calculation. *Phys. Chem. Chem. Phys.* **2015**, *17*, 10520–10531.
- (55) Pejov, L.; ngberg, D. S.; Hermansson, K.  $Al^{3+}$ ,  $Ca^{2+}$ ,  $Mg^{2+}$ , and  $Li^+$  in aqueous solution: Calculated first-shell anharmonic OH vibrations at 300 K. *J. Chem. Phys.* **2010**, *133*, 174513.
- (56) Lill, J. V.; Parker, G. A.; Light, J. C. Discrete variable representations and sudden models in quantum scattering theory. *Chem. Phys. Lett.* **1982**, *89*, 483–489.
- (57) Light, J. C.; Hamilton, I. P.; Lill, J. V. Generalized discrete variable approximation in quantum mechanics. *J. Chem. Phys.* **1985**, *82*, 14001409.
- (58) Bačić, Z.; Light, J. C. Theoretical Methods for Rovibrational States of Floppy Molecules. *Annu. Rev. Phys. Chem.* **1989**, *40*, 469–498.
- (59) Stancik, A. L.; Brauns, E. B. A simple asymmetric lineshape for fitting infrared absorption spectra. *Vib. Spectrosc.* **2008**, *47*, 66–69.
- (60) Luzar, A.; Chandler, D. Effect of Environment on Hydrogen Bond Dynamics in Liquid Water. *Phys. Rev. Lett.* **1996**, *76*, 928–931.
- (61) Benedict, W. S.; Gailar, N.; Plyler, E. K. Rotation-Vibration Spectra of Deuterated Water Vapor. *J. Chem. Phys.* **1956**, *24*, 1139–1165.
- (62) Fecko, C. J.; Eaves, J. D.; Loparo, J. J.; Tokmakoff, A.; Geissler, P. L. Ultrafast Hydrogen-Bond Dynamics in the Infrared Spectroscopy of Water. *Science* **2003**, *301*, 1698–1702.

- (63) Owrutsky, J. C.; Rosenbaum, N. H.; Tack, L. M.; Saykally, R. J. The vibration-rotation spectrum of the hydroxide anion ( $\text{OH}^-$ ). *J. Chem. Phys.* **1985**, *83*, 5338–5339.
- (64) Corridoni, T.; Sodo, A.; Bruni, F.; Ricci, M. A.; Nardone, M. Probing water dynamics with  $\text{OH}^-$ . *Chem. Phys.* **2007**, *336*, 183–187.
- (65) Ando, Y.; Gohda, Y.; Tsuneyuki, S. *Ab initio* molecular dynamics study of the Helmholtz layer formed on solid–liquid interfaces and its capacitance. *Chem. Phys. Lett.* **2013**, *556*, 9–12.
- (66) Ikeda, T. First principles molecular dynamics study of interlayer water and cations in vermiculite. *Clay Sci.* **2014**, *18*, 23–31.
- (67) Li, D.; Yang, Y.; Wang, X.; Feng, G. Electrical Double Layer of Linear Tricationic Ionic Liquids at Graphite Electrode. *J. Phys. Chem. C* **2020**, *124*, 15723–15729.
- (68) Huang, C.; Zhao, X.; Liu, S.; Hao, Y.; Tang, Q.; Hu, A.; Liu, Z.; Chen, X. Stabilizing Zinc Anodes by Regulating the Electrical Double Layer with Saccharin Anions. *Adv. Mater.* **2021**, *33*, 2100445.
- (69) Shin, S.; Kim, D. H.; Bae, G.; Ringe, S.; Choi, H.; Lim, H.; Choi, C. H.; Kim, H. On the importance of the electric double layer structure in aqueous electrocatalysis. *Nat. Commun.* **2022**, *13*, 174.
- (70) Otani, M.; Hamada, I.; Sugino, O.; Morikawa, Y.; Okamoto, Y.; Ikeshoji, T. Electrode Dynamics from First Principles. *J. Phys. Soc. Jpn.* **2008**, *77*, 024802.
- (71) Hörmann, N. G.; Guo, Z.; Ambrosio, F.; Andreussi, O.; Pasquarello, A.; Marzari, N. Absolute band alignment at semiconductor–water interfaces using explicit and implicit descriptions for liquid water. *npj Comput. Mater.* **2019**, *5*, 100.
- (72) Guo, Y.; Li, H.; Clark, S. J.; Robertson, J. Band Offset Models of Three-Dimensionally Bonded Semiconductors and Insulators. *J. Phys. Chem. C* **2019**, *123*, 5562–5570.

- (73) Sun, M.; Lu, Q.; Wang, Z. L.; Huang, B. Understanding contact electrification at liquid–solid interfaces from surface electronic structure. *Nat. Commun.* **2021**, *12*, 1752.
- (74) Wen, X.; Fan, X.; Jin, X.; Cheng, J. Band Alignment of 2D Material–Water Interfaces. *J. Phys. Chem. C* **2023**, *127*, 4132–4143.

## Supporting Information Available

Table 11: The configurations of atoms (Zr, N, O) and vacancies (V) in the unit cell of  $\text{Zr}_7\text{O}_8\text{N}_4$  and  $\text{ZrO}_2$  are shown in coordinates relative to the lattice vector.

$n_1$	$n_2$	$n_3$	atom
0.333333	0.333333	0.118933	Zr
0.476190	0.619048	0.118933	Zr
0.619048	0.904762	0.118933	Zr
0.904762	0.476190	0.118933	Zr
0.047619	0.761905	0.118933	Zr
0.761905	0.190476	0.118933	Zr
0.190476	0.047619	0.118933	Zr
0.809524	0.952381	0.237867	Zr
0.238095	0.809524	0.237867	Zr
0.523809	0.380952	0.237867	Zr
0.666667	0.666667	0.237867	Zr
0.952381	0.238095	0.237867	Zr
0.095238	0.523809	0.237867	Zr
0.380952	0.095238	0.237867	Zr
0.571429	0.142857	0.356800	Zr
0.857143	0.714286	0.356800	Zr
0.714286	0.428571	0.356800	Zr
0.000000	0.000000	0.356800	Zr
0.428571	0.857143	0.356800	Zr
0.285714	0.571429	0.356800	Zr
0.142857	0.285714	0.356800	Zr
0.904762	0.476190	0.475733	Zr
0.761905	0.190476	0.475733	Zr
0.190476	0.047619	0.475733	Zr
0.619048	0.904762	0.475733	Zr
0.476190	0.619048	0.475733	Zr
0.047619	0.761905	0.475733	Zr
0.333333	0.333333	0.475733	Zr
0.952381	0.238095	0.594667	Zr
0.238095	0.809524	0.594667	Zr
0.095238	0.523809	0.594667	Zr
0.523809	0.380952	0.594667	Zr
0.666667	0.666667	0.594667	Zr
0.809524	0.952381	0.594667	Zr
0.380952	0.095238	0.594667	Zr

Table 12: Continued from Table 11

$n_1$	$n_2$	$n_3$	atom
0.000000	0.000000	0.089200	O
0.571429	0.142857	0.089200	O
0.857143	0.714286	0.089200	O
0.714286	0.428571	0.089200	O
0.428571	0.857143	0.089200	V(O)
0.285714	0.571429	0.089200	O
0.142857	0.285714	0.089200	O
0.380952	0.095238	0.148667	O
0.952381	0.238095	0.148667	N(O)
0.238095	0.809524	0.148667	O
0.095238	0.523809	0.148667	V(O)
0.809524	0.952381	0.148667	N(O)
0.666667	0.666667	0.148667	O
0.523809	0.380952	0.148667	O
0.047619	0.761905	0.208133	O
0.333333	0.333333	0.208133	N(O)
0.476190	0.619048	0.208133	N(O)
0.904762	0.476190	0.208133	O
0.761905	0.190476	0.208133	V(O)
0.190476	0.047619	0.208133	N(O)
0.619048	0.904762	0.208133	N(O)
0.000000	0.000000	0.267600	O
0.571429	0.142857	0.267600	N(O)
0.714286	0.428571	0.267600	N(O)
0.857143	0.714286	0.267600	O
0.142857	0.285714	0.267600	O
0.285714	0.571429	0.267600	O
0.428571	0.857143	0.267600	V(O)
0.952381	0.238095	0.327067	O
0.380952	0.095238	0.327067	O
0.523809	0.380952	0.327067	O
0.238095	0.809524	0.327067	O
0.095238	0.523809	0.327067	V(O)
0.666667	0.666667	0.327067	N(O)
0.809524	0.952381	0.327067	O

Table 13: Continued from Table 12

$n_1$	$n_2$	$n_3$	atom
0.190476	0.047619	0.386533	O
0.761905	0.190476	0.386533	V(O)
0.904762	0.476190	0.386533	N(O)
0.047619	0.761905	0.386533	O
0.333333	0.333333	0.386533	O
0.619048	0.904762	0.386533	N(O)
0.476190	0.619048	0.386533	N(O)
0.714286	0.428571	0.446000	O
0.571429	0.142857	0.446000	O
0.000000	0.000000	0.446000	O
0.142857	0.285714	0.446000	O
0.857143	0.714286	0.446000	N(O)
0.428571	0.857143	0.446000	V(O)
0.285714	0.571429	0.446000	N(O)
0.095238	0.523809	0.505467	V(O)
0.952381	0.238095	0.505467	N(O)
0.380952	0.095238	0.505467	N(O)
0.238095	0.809524	0.505467	N(O)
0.809524	0.952381	0.505467	O
0.523809	0.380952	0.505467	O
0.666667	0.666667	0.505467	N(O)
0.190476	0.047619	0.564933	O
0.761905	0.190476	0.564933	V(O)
0.333333	0.333333	0.564933	N(O)
0.476190	0.619048	0.564933	O
0.047619	0.761905	0.564933	N(O)
0.904762	0.476190	0.564933	O
0.619048	0.904762	0.564933	O
0.714286	0.428571	0.624400	O
0.857143	0.714286	0.624400	O
0.571429	0.142857	0.624400	O
0.000000	0.000000	0.624400	O
0.142857	0.285714	0.624400	O
0.285714	0.571429	0.624400	O
0.428571	0.857143	0.624400	V(O)